

1           **Precipitating electron energy spectra and auroral**  
2           **power estimation by incoherent scatter radar with high**  
3           **temporal resolution**

4           **Habtamu W. Tesfaw**<sup>1</sup>, **Ilkka I. Virtanen**<sup>1</sup>, **Anita Aikio**<sup>1</sup>, **Amoré Nel**<sup>2</sup>, **Michael**  
5           **Kosch**<sup>2,3,4</sup>, and **Yasunobu Ogawa**<sup>5</sup>

6                           <sup>1</sup>Space Physics and Astronomy Research Unit, University of Oulu, Oulu, Finland

7                           <sup>2</sup>South African National Space Agency, Hermanus, South Africa

8                           <sup>3</sup>Physics Dept., Lancaster University, Lancaster, UK

9                           <sup>4</sup>Dept. of Physics and Astrophysics, University of Western Cape, Bellville, South Africa

10                           <sup>5</sup>National Institute of Polar Research, Tokyo, Japan

11           **Key Points:**

- 12           • We use the BAFIM-ELSPEC analysis combination to calculate the energy spec-  
13           tra of precipitating electrons with high time resolution.
- 14           • Using the fitted electron density data in precipitation events leads to wider en-  
15           ergy spectra, and larger auroral power and FAC estimates.
- 16           • Auroral power calculated using the BAFIM-ELSPEC analysis agrees very well with  
17           that of the 427.8 nm emission line intensity.

---

Corresponding author: Habtamu W. Tesfaw, [Habtamu.Tesfaw@oulu.fi](mailto:Habtamu.Tesfaw@oulu.fi)

18 **Abstract**

19 This study presents an improved method to estimate differential energy flux, au-  
 20 roral power and field-aligned current of electron precipitation from incoherent scatter radar  
 21 data. The method is based on a newly developed data analysis technique that uses Bayesian  
 22 filtering to fit altitude profiles of electron density, electron temperature, and ion temper-  
 23 ature to observed incoherent scatter spectra with high time and range resolutions. The  
 24 electron energy spectra are inverted from the electron density profiles. Previous high-  
 25 time resolution fits have relied on the raw electron density, which is calculated from the  
 26 backscattered power assuming that the ion and electron temperatures are equal. The im-  
 27 proved technique is applied to one auroral event measured by the EISCAT UHF radar  
 28 and it is demonstrated that the effect of electron heating on electron energy spectra, au-  
 29 roral power and upward field-aligned current can be significant at times. Using the fit-  
 30 ted electron densities instead of the raw ones may lead to wider electron energy spec-  
 31 tra and auroral power up to 75% larger. The largest differences take place for precip-  
 32 itation that produces enhanced electron heating in the upper E region, and in this study  
 33 correspond to fluxes of electrons with peak energies from 3 to 5 keV. Finally, the auro-  
 34 ral power estimates are verified by comparison to the 427.8 nm auroral emission inten-  
 35 sity, which show good correlation. The improved method makes it possible to calculate  
 36 unbiased estimates of electron energy spectra with high time resolution and thereby to  
 37 study rapidly varying aurora.

38 **1 Introduction**

39 Electron precipitation to the high-latitude ionosphere is a key process in magnetosphere-  
 40 ionosphere coupling and in the physics of the mesosphere-lower thermosphere (MLT) re-  
 41 gion, because the precipitating electrons carry electric current, transfer energy from the  
 42 magnetosphere to the ionosphere, ionize neutral atoms and molecules, cause optical au-  
 43 roral emissions, heat the electron gas, and change the ion composition. High resolution  
 44 observations are needed in studies of these phenomena, as the processes often take place  
 45 in small spatial and temporal scales.

46 Electron precipitation is quantitatively characterized by the energy distribution of  
 47 the primary electrons. Electron acceleration processes in the magnetosphere that lead  
 48 to different energy spectral shapes are discussed by Newell et al. (2009) and Dombeck  
 49 et al. (2018). For a known differential energy flux, altitude profiles of ion production rate  
 50 and auroral emission rates can be determined if the neutral atmospheric parameters are  
 51 known (Rees, 1963; Fang et al., 2010).

52 Indirect estimation of the differential energy flux from electron density altitude pro-  
 53 files observed with an incoherent scatter radar (ISR) is an efficient way to observe elec-  
 54 tron precipitation from ground (Vondrak & Baron, 1977; Kirkwood, 1988; Brekke et al.,  
 55 1989; Semeter & Kamalabadi, 2005; Kaeppler et al., 2015; Simon Wedlund et al., 2013;  
 56 Virtanen et al., 2018). Unlike in situ observations with fast moving satellites and rock-  
 57 ets, the radar observations allow one to follow the time evolution of the electron precip-  
 58 itation along the local geomagnetic field.

59 Two different analysis techniques are commonly used to obtain electron densities  
 60 from an ISR observation. Scaling the backscattered power with radar system param-  
 61 eters results in the so-called raw electron density ( $N_r$ ), which is equal to the actual elec-  
 62 tron density ( $N_e$ ) if electron and ion temperatures are equal. A more sophisticated way  
 63 is to make a least-squares fit of a parametric incoherent scatter spectrum model to the  
 64 observed spectra. Typically, electron density ( $N_e$ ), electron temperature ( $T_e$ ), ion tem-  
 65 perature ( $T_i$ ), and line-of-sight ion bulk velocity ( $V_i$ ) are fitted.

66 The electron density profiles need to be observed with high resolutions in range and  
 67 time to enable accurate estimation of the rapidly varying electron energy spectra. While  
 68 plasma parameter fits to EISCAT ISR data are typically made with a few kilometer range  
 69 resolution and some tens of seconds time resolution using the Grand Unified Incoher-  
 70 ent Scatter Design and Analysis Package (GUISDAP) (Lehtinen & Huuskonen, 1996),  
 71 the electron energy spectra fits require range resolution better than 2 km (Semeter &  
 72 Kamalabadi, 2005) and time resolution of the order of five seconds (Virtanen et al., 2018).

73 Since other high-latitude ISR facilities cannot produce better resolutions either, previ-  
 74 ous high time resolution energy spectrum fits have been based on raw electron den-  
 75 sities (Burns et al., 1990; Lanchester et al., 1994, 1996, 1997; Semeter & Kamalabadi,  
 76 2005; Dahlgren et al., 2011; Virtanen et al., 2018), while the fitted electron densities have  
 77 been used with 1 min or coarser resolutions (Hargreaves & Devlin, 1990; Kirkwood &  
 78 Eliasson, 1990; Strickland et al., 1994; Fujii et al., 1995; Osepian & Kirkwood, 1996; Kosch  
 79 et al., 2001; Kaeppler et al., 2015). However, the electron precipitation tends to heat the  
 80 electron gas, which makes the implicit assumption of  $T_e = T_i$  questionable in calcula-  
 81 tion of  $N_r$ . The raw density  $N_r$  is smaller than the actual density  $N_e$  if  $T_e > T_i$ , which  
 82 may lead to underestimation of the precipitating energy flux if  $N_r$  is used in electron en-  
 83 ergy spectrum fits.

84 An optical signature of the electron precipitation are auroral emissions, which are  
 85 produced when excited atoms, molecules, and ions return to their ground states. Op-  
 86 tical observations are vital to complement the radar observations and to put them into  
 87 wider context. While optical observations lack the altitude information provided by radars,  
 88 they can image the auroral emissions in 2D and can reach angular and time resolutions  
 89 superior to those of the radars. Energy flux of the precipitating electrons can also be in-  
 90 ferred from the auroral blue line (427.8 nm) emission intensity which is emitted by re-  
 91 laxation of excited  $N_2^+$  molecular ions. Previous studies have shown direct proportion-  
 92 ality between line of sight integrated blue line emission intensity and total energy flux  
 93 of the precipitating electrons (Omholt, 1971; Rees & Luckey, 1974; Strickland et al., 1989;  
 94 Partamies et al., 2004).

95 Recently, Kaeppler et al. (2015) have made comparisons between radar and opti-  
 96 cal observations, in which the energy flux is calculated from a fitted electron density data  
 97 with 4.5 km range, and 1 and 3 min time resolutions. Their focus was on stable auro-  
 98 ral features. On the other hand, in a study by Lanchester et al. (1997) the energy flux  
 99 corresponding to a dynamic auroral structure was derived from the blue line emission  
 100 intensity data measured with sub-second (0.2 s) temporal resolution. The authors adjusted  
 101 the derived energy flux against a high resolution (0.2 s) raw electron density data ob-  
 102 tained from the EISCAT UHF radar observation.

103 The aim of this study is to introduce an improved method to calculate energy spec-  
 104 tra of auroral electrons from ISR measurements with high time resolution. We perform  
 105 full four-parameter fits to the observed incoherent scatter spectra with high resolutions  
 106 in time and range and use the actual fitted  $N_e$  in high-resolution electron energy spec-  
 107 trum inversion for the first time. Using the fitted electron density in the inversion re-  
 108 moves a bias in the fitted energy spectra that occurs during electron heating events if  
 109 the raw electron density is used.

110 The high-resolution plasma parameter fit is possible with the newly developed Bayesian  
 111 Filtering Module (BAFIM) (Virtanen et al., 2021). BAFIM makes use of smoothness pri-  
 112 ors in time and range (along the geomagnetic field line) for the plasma temperature pro-  
 113 files to reach high resolution in the electron density fits, as described in Section 4.1. Elec-  
 114 tron energy spectra are then inverted from the BAFIM-fitted electron density profiles  
 115 using a method developed by Virtanen et al. (2018) known as ELSPEC (ELECTRON SPEC-  
 116 TRUM) and described in Section 4.3. ELSPEC uses parametric models for the electron  
 117 energy spectra, models the ion production and loss rates, and solves the electron den-

118 sity as function of time from its continuity equation. Difference between the modeled elec-  
 119 tron density profile and the radar observation is then iteratively minimized to find the  
 120 best matching electron energy spectra.

121 The BAFIM-ELSPEC analysis combination is applied to an auroral event that com-  
 122 prises wide range of auroral features. By comparing the ELSPEC analysis results ob-  
 123 tained from the fitted and raw electron densities, we study effects of enhanced electron  
 124 heating on the calculated energy spectra of the precipitating electrons. To validate our  
 125 auroral power estimates, we compare the auroral power (total energy flux) calculated from  
 126 the BAFIM-ELSPEC analysis combination with that of the 427.8 nm spectral (blue) line  
 127 emission intensity.

128 The paper is organized as follows; data and measurements are introduced in Sec-  
 129 tion 2, the auroral event is described in Section 3, the radar data analysis and the ef-  
 130 fect of electron heating are discussed in Section 4, and auroral power derived from the  
 131 radar observations is compared to optical observations in Section 5. Discussion and sum-  
 132 mary are presented in Section 6.

## 133 2 Data and Measurements

134 The active auroral event presented in this study took place on 9 March 2016, 19:40  
 135 - 23:40 UT over Tromsø, Norway. The EISCAT UHF radar near Tromsø (69.58°N, 19.23°E  
 136 Geodetic, and 66.67°N, 101.41°E Geomagnetic) was pointed along the local geomagnetic  
 137 field and it was running the 'arc1' experiment, which uses a 64-bit alternating code se-  
 138 quence (Lehtinen & Häggström, 1987) with 6  $\mu$ s bit length. The 128 pulses of the code  
 139 sequence were transmitted with 3.468 ms inter-pulse periods, and autocorrelation func-  
 140 tion data decoded to 900 m range resolution were stored from each 443.9 ms long pulse  
 141 sequence. In this study we use data integrated to 4 s time resolution.

142 In addition to the ISR observations, we characterize the dynamics of the observed  
 143 auroral structures using all-sky camera (ASC) and narrow field of view optical observa-  
 144 tions. All-sky images of the auroral green line emission (557.7 nm) with 1 s time reso-  
 145 lution are obtained from the Watec monochromatic imager (WMI) (Ogawa et al., 2020)  
 146 located at the EISCAT Tromsø radar site. In addition, we use an EMCCD imager lo-  
 147 cated at the radar site (Nel et al., 2021) for narrow field of view (FoV) observations of  
 148 small-scale auroral structures around and within the radar beam. The detector images  
 149 auroral emissions at wavelength 427.8 nm with a 30° FoV and 3 s exposure time. The  
 150 camera system was pointing to the geomagnetic zenith.

151 Local and global (Nose et al., 2015) auroral electrojet indices are also used to mon-  
 152 itor the geomagnetic activity. Geomagnetic field data obtained from the IMAGE net-  
 153 work of magnetometers are used to derive the local auroral electrojet (IL) index (Kallio  
 154 et al., 2000). Finally, an induction coil magnetometer at Kilpisjärvi (69.06°N, 20.77°E  
 155 Geodetic, and 66.07°N, 102.30°E Geomagnetic) is used to monitor the geomagnetic pul-  
 156 sation activity.

## 157 3 Event Description

158 Overview of the event is given in Figure 1. A time lapse video of the ASC and nar-  
 159 row FoV auroral images is provided as a supplementary material. The raw electron den-  
 160 sity obtained from the EISCAT UHF radar observation is placed in the first panel of the  
 161 figure. Keograms produced from the North-South cut of the narrow FoV and ASC au-  
 162 roral images over the radar zenith are shown in the second and third panels, respectively.  
 163 We make coordinate transformation at 110 km to calculate the latitudes for the keograms.  
 164 The horizontal white lines in the keograms represent position of the radar beam. Power  
 165 spectra of geomagnetic pulsations, and local (IL) and global (AL) auroral electrojet in-

166  
167

lices are shown in the fourth and fifth panels, respectively. Selected all-sky auroral images are shown in Figure 2. Magnetic midnight at Tromsø is at about 21:30 UT.

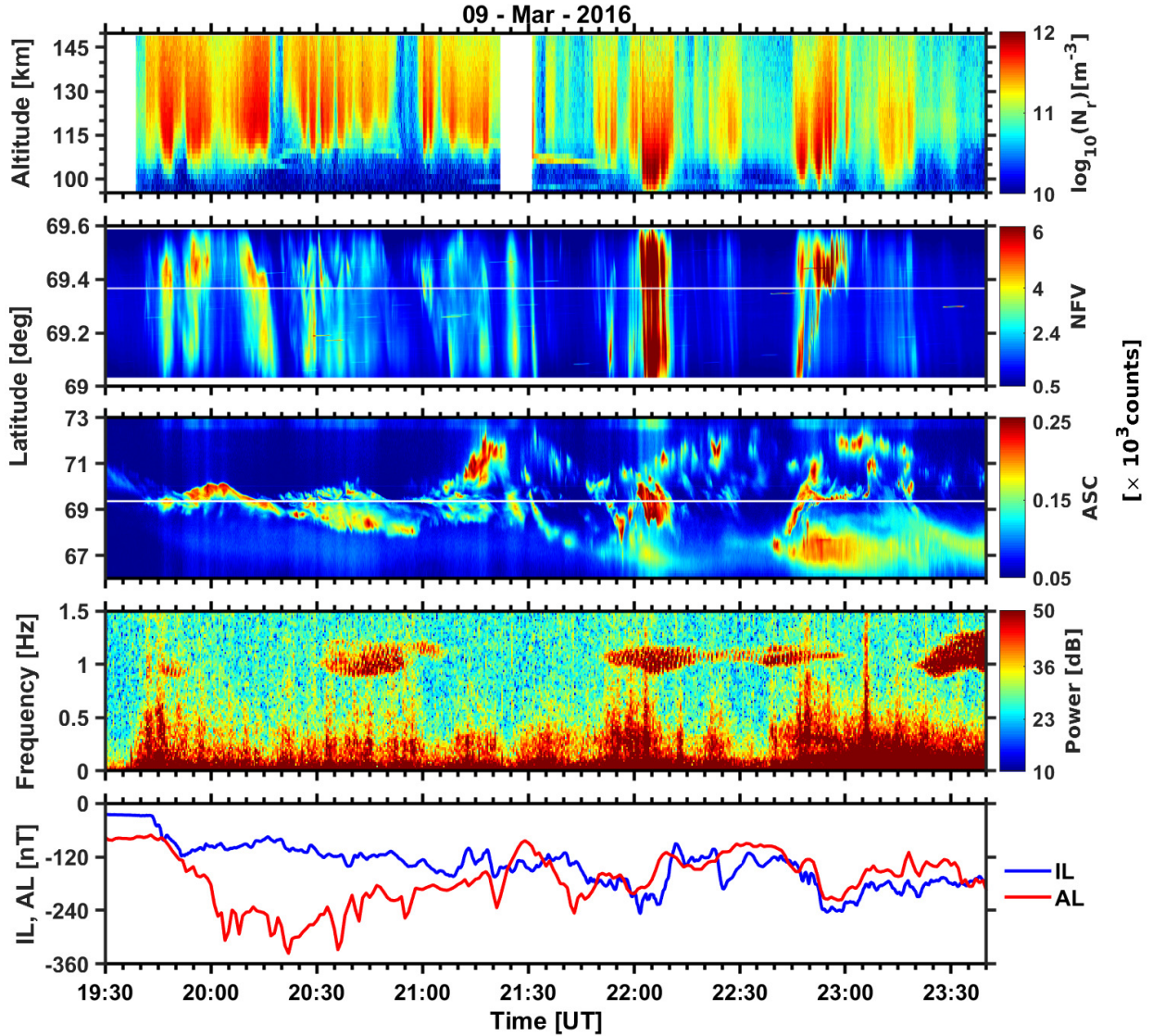


**Figure 1.** An overview of the auroral event. Panels from top to bottom: raw electron density, narrow FoV keogram (427.8 nm), ASC Keogram (557.7 nm), geomagnetic pulsation spectrogram, and IL and AL electrojet indices.

168  
169  
170  
171  
172  
173  
174

At 19:30 UT there were several faint arcs in the FoV of the ASC which later drifted equatorward. After few minutes, at about 19:39 UT, the first signature of an intensification of an arc is seen in the eastern horizon. At about the same time, the peak frequency in the pulsation power spectrum jumps from below 1 mHz to about 0.5 Hz, which indicates development of PiB pulsations (McPherron, 2005; Olson, 1999). PiB pulsation development and sudden brightening of auroral arcs are typical indicators of substorm activation (Sakurai & Saito, 1976; Mishin et al., 2020). The IL and AL indices decrease

175 abruptly at about 19:40, which is another indication of substorm onset (Tanskanen, 2009;  
176 Hsu & McPherron, 2012).

177 Based on the AL index, three relatively small substorm onsets took place during  
178 the studied time interval with rough onset times at 19:40, 21:30 and 22:40 UT. During  
179 the first substorm, the IL index remained much smaller than the AL index indicating  
180 that the substorm onset region was not in Scandinavia, but rather to the east, closer to  
181 magnetic midnight.

182 In addition to the continuous PiB activity, magnetic pulsations show signatures of  
183 Pc1 pulsations near 1 Hz, which are produced by protons injected to the inner magne-  
184 tosphere and interacting with ion cyclotron waves (Saito, 1969). It is probable that this  
185 injection is a consequence of substorm onset.

186 The radar starts recording large ionization enhancements after 19:44 UT when the  
187 most equatorward arc, which was within the radar beam, became bright. This wide bright  
188 auroral arc stays within the beam until 19:51 UT, as shown in auroral images A and B  
189 of Figure 2, and produces the first period of enhanced ionization between 19:44 and 19:51 UT.  
190 The arc then fades in its intensity, and by 19:52 UT it is substituted by several east-west  
191 aligned arcs forming together a bright bulge that expands poleward. Selected images of  
192 the bulge are shown in panels C and D of Figure 2.

193 Probing the poleward advancing bulge, the radar measures an ionization enhance-  
194 ment between 19:52 and 20:00 UT. The bulge leaves the radar beam at about 20:01 UT  
195 and continues expanding poleward until 20:04 UT. Then it starts to retreat from its pole-  
196 ward extent and advances equatorward across the radar beam. As indicated in auroral  
197 images E and F of Figure 2, the radar was observing the equatorward moving arc be-  
198 tween 20:07 and 20:16 UT to produce the third ionization enhancement. The east-west  
199 aligned arc continued drifting equatorward and left the radar beam at about 20:16:30 UT.

200 At about 20:22 UT, the AL index attained its minimum value of about -350 nT,  
201 indicating the end of the first substorm expansion phase. During the first substorm re-  
202 covery phase, between 20:20 and 21:30, multiple auroral features with folds and curls are  
203 created across the auroral oval as shown in the ASC and narrow FoV keograms in Fig-  
204 ure 1. Sample auroral images taken from this time interval are shown in panels G and  
205 H of Figure 2. When these auroral structures perform radar beam crossings, series of sev-  
206 eral short lived ionization enhancements are produced between 20:20 and 21:20 UT.

207 During the first substorm, all the arcs were streaming mostly towards the west. Counter-  
208 streaming arcs were also observed so that in the northern part the streaming was to the  
209 east and in the southern part towards the west, indicating converging electric field struc-  
210 ture and auroral potential drop above the the ionosphere (Carlson et al., 1998; Aikio et  
211 al., 2002). We also find the energy spectra of the electron flux corresponding to these  
212 arcs to be in the form of inverted-V type structures.

213 Following break up of the second substorm at about 21:30 UT, a bright auroral fea-  
214 ture is seen in the north-west horizon of the ASC at about 21:35 UT, indicating the on-  
215 set region of this substorm was to the west of Tromsø. After the onset, the streaming  
216 inside the arcs becomes mainly eastward. Eventually a bright auroral bulge, expanding  
217 to the ASC FoV from the west, is formed at about 21:57 UT. Selected images of the bulge  
218 are shown in panels I and J of Figure 2. When the bulge passes through the radar beam  
219 at about 21:59, it produces an electron density enhancement characterized by largest peak  
220 electron densities (in the order of  $10^{12} \text{ m}^{-3}$ ) and lowest peak altitudes (about 100 km)  
221 of the event. The narrow FoV and ASC keograms show that the radar beam was at the  
222 center of this intensifying bulge from 22:00 until 22:11 UT. The auroral bulge fades in  
223 its intensity by 22:12. After that and until 22:40 several auroral features with varying  
224 luminosity are observed across the horizon of the ASC.

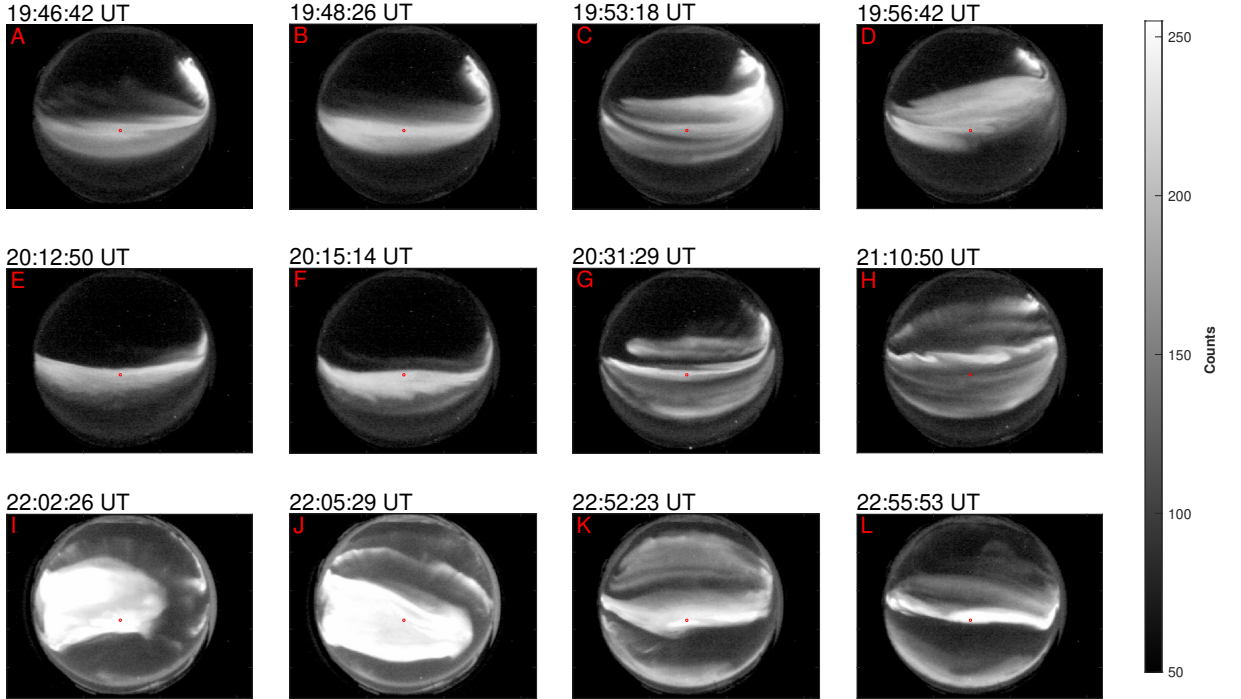


**Figure 2.** Selected auroral images taken from the ASC camera observation on 9 March, 2016. The radar beam is shown as a red dot in the images. North is up and east is to the right.

225 The AL index shows that onset of the third substorm occurs at about 22:40 UT.  
 226 Indeed, at 22:39 UT an auroral arc was observed intensifying from west to east in the  
 227 very southern horizon of the ASC, indicating the onset was to the west of Scandinavia.  
 228 Auroral images K and L of Figure 2 show that the radar measured the last ionization  
 229 enhancement between 22:44 and 22:56 UT when these auroral arcs drift poleward. ASC  
 230 and narrow FoV keograms indicate that the radar was observing the equatorward edge  
 231 of an east west aligned auroral arc between 22:53 and 22:56 UT.

232 In addition to ionization by precipitating electrons, sporadic E layers can be seen  
 233 during two time intervals in the electron density plot. The first sporadic E layer is ob-  
 234 served between 20:20 and 20:52 UT in the altitude regions of 109 km, and the second  
 235 one is between 21:30 and 21:48 UT at about 106 km.

#### 236 4 Electron Energy Spectrum Analysis

237 The analysis method we use to calculate the differential electron energy flux from  
 238 the EISCAT UHF ISR data consists of two steps. First, plasma parameters are fitted  
 239 to the incoherent scatter data with high time and range resolutions using the combina-  
 240 tion of GUIDAP (Lehtinen & Huuskonen, 1996) and BAFIM (Virtanen et al., 2021).  
 241 Second, the fitted electron density altitude profiles are inverted into differential energy  
 242 fluxes of precipitating electrons using the ELSPEC software (Virtanen et al., 2018). In  
 243 this section, we introduce the analysis methods and address the effect of electron heat-  
 244 ing on the raw electron density  $N_r$  for the first substorm discussed in Section 3. We con-  
 245 sider both the bias in raw electron density and its effects on the electron energy spec-  
 246 trum fits.

247

#### 4.1 Fitted and raw electron densities

248

249

250

251

252

253

254

255

256

257

258

259

260

In the traditional 'gated' incoherent scatter plasma parameter fits, one averages the incoherent scatter autocorrelation function (ACF) over selected intervals in range and time, and fits the plasma parameters to the averaged autocorrelation functions in each range-gate and time-step. Each fit is independent of the others and one cannot include prior information about shape of the plasma parameter profiles, or about their expected temporal variations. Statistical accuracy of the fitted plasma parameters depends on the resolutions, since accuracy of the observed ACF is improved with increasing integration in time or range. The standard GUIDAP analysis of EISCAT radar data uses the gated analysis principle. Accuracy of the GUIDAP fit results depends also on the level of ionization in the observed region, which affects the signal-to-noise ratio. Although E region electron density is typically high during active aurora, resolutions needed to follow the associated rapid variations in electron energy spectra are practically out of reach of the standard four-parameter fits of  $N_e$ ,  $T_e$ ,  $T_i$ , and  $V_i$  with GUIDAP.

261

262

263

264

265

266

267

Due to the limitations of the four-parameter fits, the high-resolution electron density observations are typically based on the raw electron density, which is the backscattered signal power multiplied with radar system parameters. Assuming that the Debye length is much smaller than the radar wavelength, which is a well justified assumption in E region observations with the EISCAT UHF radar, the relation between the raw density  $N_r$  and the actual density  $N_e$  can be written as (Baron, 1977; Semeter & Kamalabadi, 2005),

$$N_r = \frac{2N_e}{(1 + T_r)}, \quad (1)$$

268

269

270

271

272

273

274

where  $T_r = T_e/T_i$ . Obviously,  $N_e = N_r$  when  $T_r = 1$ , but  $N_e > N_r$  when  $T_r > 1$ . For example,  $N_e = 1.5 \cdot N_r$  if  $T_r = 2$ , which is not an unusual temperature ratio in the upper E region during electron precipitation. Auroral events with enhanced E region electron temperature have been investigated e.g. by Wickwar et al. (1981), who found that the electron density altitude profiles calculated with correct temperature ratio have lower peak altitudes and greater peak electron densities than those of the raw electron density altitude profiles.

275

276

277

278

279

280

281

282

283

284

285

286

287

288

289

290

291

An alternative to the gated analysis is the full-profile analysis (Holt et al., 1992; Lehtinen et al., 1996; Hysell et al., 2008), in which one fits full range-profiles of plasma parameters. The full-profile analysis allows one to include prior information about the plasma parameter profiles, but it is also computationally heavier than the gated analysis. The Bayesian Filtering Module (BAFIM) (Virtanen et al., 2021) is an extension module to GUIDAP, which allows one to include prior information about plasma parameter gradients in both range and time in the gated GUIDAP analysis. BAFIM thus extends the idea of full profile analysis to smoothness in both range and time, but without increasing the computational burden of the gated analysis. BAFIM introduces correlations in between adjacent range-gates and time-steps in a way that leads to effectively coarser resolutions in range and time than those defined by the range-gates and time-steps. Since the correlations are defined for each plasma parameter separately, one can use effectively coarser resolutions for  $T_e$ ,  $T_i$ , and  $V_i$ , but fit the electron density  $N_e$  with the best possible resolution. The assumption of smoothness in the  $T_e$  and  $T_i$  profiles is justified in field-aligned observations, because the high mobility along the magnetic field prevents generation of large field-aligned temperature gradients in the upper E and lower F regions.

292

#### 4.2 High resolution plasma parameter fit with BAFIM

293

294

295

For this study, we ran a BAFIM fit of  $N_e$ ,  $T_e$ ,  $T_i$ , and  $V_i$  on the EISCAT UHF radar data with 1.8 km range steps and 4 s time steps. BAFIM was tuned so that the "effective" time and range resolutions of  $N_e$  are very close to the time and range steps, while

296 resolutions of the other plasma parameters are effectively coarser. Interested readers are  
 297 referred to Table 1 of Virtanen et al. (2021) for the values of the tuned analysis param-  
 298 eters and their physical meanings. For this particular study, however, we changed the  
 299 electron density correlation length ( $s^h$ ) and process noise ( $s^t$ ) scaling parameters to 0.1  
 300 and  $1.0 \cdot 10^{12} \text{ m}^{-3} \text{ s}^{-1/2}$ , respectively. The 1.8 km resolution was chosen, because it pro-  
 301 duces better temperature estimates than the 0.9 km resolution, and the change from 0.9 km  
 302 to 1.8 km resolution did not affect results of the subsequent ELSPEC analysis. The raw  
 303 electron density is first calculated from the same data with 0.9 km range resolution and  
 304 4 s time resolution, and then integrated in range to 1.8 km range resolution to match  
 305 the corresponding resolution of the BAFIM analysis. The alternating code experiment  
 306 does not provide true backscattered powers, but the raw density is calculated from a short  
 307 non-zero lag of the autocorrelation function.

308 In order to demonstrate the bias in the raw electron density and its subsequent ef-  
 309 fect on the energy spectra analysis, we choose for the analysis expansion phase of the  
 310 first substorm during which pronounced electron heating was observed. The electron den-  
 311 sity ( $N_e$ ) and temperature ratio ( $T_e/T_i$ ) fit results obtained from the BAFIM analysis  
 312 are placed in the first and fourth panels of Figure 3, respectively. The raw electron den-  
 313 sity ( $N_r$ ) is shown in second panel of the figure. The difference  $N_e - N_r$  is shown in the  
 314 third panel. As shown in the first and second panels of Figure 3, three intervals of en-  
 315 hanced ionization can be identified from the electron density plots, which are associated  
 316 to specific auroral features discussed in Section 3.

317 As shown by the bottom panel of the figure, time intervals with  $T_r > 1$  match with  
 318 the periods of enhanced ionization. These concurrent enhancements indicate that the  
 319 energy deposited during the course of precipitation is the cause of the observed electron  
 320 gas heating. A well established elevation in the electron temperature ( $T_r > 1$ ) can be iden-  
 321 tified, on average, above about 115 km during all periods of enhanced ionization. In ad-  
 322 dition,  $T_r$  is shown to increase substantially with altitude to values greater than 1.5 above  
 323 130 km during each period of enhanced ionization. Below 103 km we do not fit the tem-  
 324 perature ratio, rather we assume  $T_r = 1$ , which is a valid assumption since collision bal-  
 325 ances the ion and electron temperatures at these altitudes.

326 The third panel of Figure 3 shows significant differences between the BAFIM elec-  
 327 tron density and raw electron density estimates during times of electron heating, i.e. when  
 328  $T_r > 1$ . Substantial difference (of the order of  $10^{11} \text{ m}^{-3}$ ) can be identified down to 115 km  
 329 altitude during each period of enhanced ionization. The observed differences increase sub-  
 330 stantially with altitude and reach about 50% close to 150 km altitude. On the other hand,  
 331 although the ionization enhancements extend down to 100 km altitude, the difference  
 332 between BAFIM-fitted and raw electron densities is insignificant below 115 km. This is  
 333 because frequent collisions balance the electron, ion, and neutral temperatures at these  
 334 altitudes.

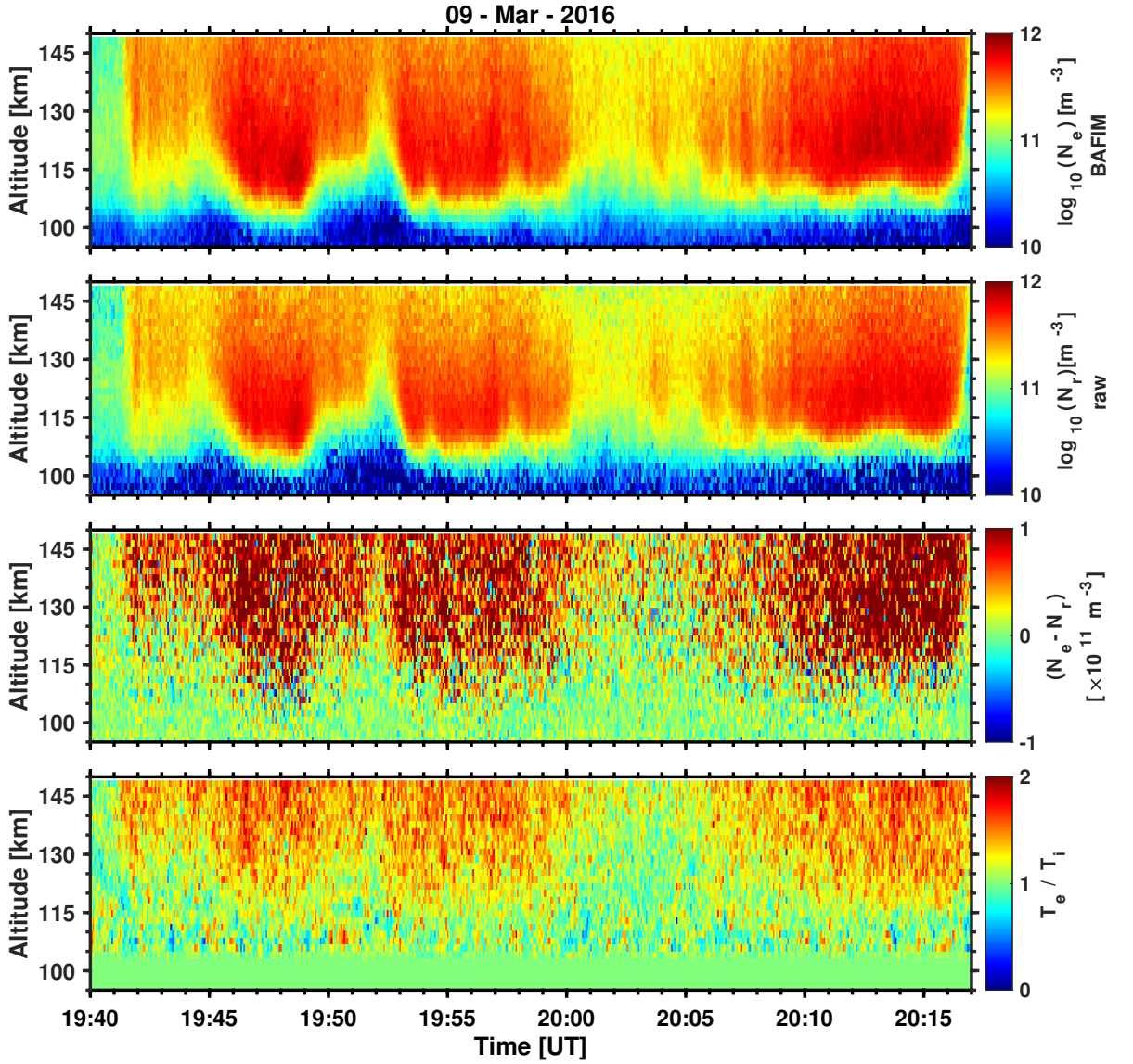


**Figure 3.** Comparison of the raw electron density  $N_r$  and the BAFIM-fitted density  $N_e$ . Panels from top to bottom: BAFIM  $N_e$ , raw density  $N_r$ , Difference  $N_e - N_r$ , and temperature ratio  $T_e/T_i$  from the BAFIM fit.

335

### 4.3 Electron energy spectrum fit with ELSPEC

336

337

338

339

We use the ELSPEC software (Virtanen et al., 2018) to invert the electron density altitude profiles into differential number flux of the precipitating electrons. ELSPEC solves the electron continuity equation that involves time derivative of the electron density, the ion production ( $Q$ ) and loss ( $L = \alpha N_e^2$ ) rates,

$$\frac{dN_e}{dt} = Q - \alpha N_e^2. \quad (2)$$

340 Ion production by mono-energetic electron beams is calculated using the model of  
 341 Fang et al. (2010), and the ion production by electrons with wide energy spectrum is cal-  
 342 culated as a sum of monoenergetic contributions at selected energy bins. The effective  
 343 recombination coefficient  $\alpha$  as function of ion composition and electron temperature is  
 344 from Sheehan & St.-Maurice (2004), where the ion composition is from the International  
 345 Reference Ionosphere (Bilitza et al., 2017) and the electron temperature is from EISCAT  
 346 ISR measurements. ELSPEC solves the electron density as function of time from the elec-  
 347 tron continuity equation (2), assuming that  $\alpha$  and the electron flux remain constant dur-  
 348 ing a radar integration, and iteratively minimizes the difference between the modeled and  
 349 measured electron density profiles. The fit is performed for a number of different spec-  
 350 trum models in each time step, and the optimal model is selected using the Akaike in-  
 351 formation criterion (Burnham & Anderson, 2002). The technique is targeted for auro-  
 352 ral electrons with energies between 1 and 100 keV, which ionize the atmosphere between  
 353 80 and 150 km altitudes.

354 Originally, ELSPEC used raw electron densities ( $N_r$ ) as input to high resolution  
 355 analysis, because the four-parameter fits were not possible with high resolutions. The  
 356 electron temperature data needed for the recombination speed calculations was taken  
 357 from standard GUIDAP fits with 60 s time and a few km range resolutions, and inter-  
 358 polated to the time and range resolutions of the raw electron density. In this study, we  
 359 use the BAFIM-fitted high-resolution (4 s/1.8 km)  $N_e$  and  $T_e$  as inputs to ELSPEC for  
 360 the first time. In order to study how much the fitted energy spectra change when the  
 361 raw electron density  $N_r$  is replaced with the fitted  $N_e$ , we ran the ELSPEC analysis also  
 362 with the raw density  $N_r$  as input.

#### 363 4.4 Effect of electron heating on energy spectrum fit

364 We applied the ELSPEC analysis on the raw and BAFIM-fitted electron densities  
 365 shown in Figure 3 to demonstrate the effect of electron heating on the electron energy  
 366 spectra fits. This time interval corresponds to the expansion phase of the first substorm  
 367 during which enhanced electron gas heating was observed for several minutes. Figure 4  
 368 shows comparison of the ELSPEC fit results with raw density  $N_r$  and fitted density  $N_e$   
 369 as inputs. From top to bottom, the panels are the BAFIM-fitted electron density ( $N_e$ ),  
 370 the differential energy flux inverted from the BAFIM  $N_e$  ( $I_b$ ), the differential energy flux  
 371 inverted from the raw density  $N_r$  ( $I_r$ ), peak energy ( $E_0$ ), auroral power, and field aligned  
 372 current (FAC). The peak energy is the energy at which the differential energy flux reaches  
 373 its maximum value. The auroral power, which is equal to the total energy flux, is cal-  
 374 culated by integrating the differential energy flux over all energies above 1 keV. The field-  
 375 aligned current is proportional to the total number flux, which is calculated by integrat-  
 376 ing the differential number flux. The FAC estimate represents the upward electric cur-  
 377 rent carried by the downward precipitating electrons with energies larger than 1 keV.  
 378 The ELSPEC FAC estimates are thus merely lower limits for the total FAC, in which  
 379 the contribution of low-energy electrons could be significant.

380 Comparing the second and third panels of Figure 4, wider energy distribution is  
 381 observed in the energy spectra calculated from BAFIM  $N_e$  than in the one obtained from  
 382 raw density  $N_r$ . Specifically, larger flux is observed in the lower energy ends of  $I_b$  than  
 383 in that of  $I_r$ . On the other hand, the peak energy obtained from raw density  $N_r$  slightly  
 384 exceeds the one obtained from BAFIM  $N_e$  (4<sup>th</sup> panel). This is another indication that  
 385 the energy distribution obtained from BAFIM  $N_e$  tends to have a larger electron flux  
 386 at its lower energies. The larger flux at lower energy ends of  $I_b$  account for  $N_e > N_r$   
 387 above 115 km altitude, as discussed in Section 4.2.

388 The 5<sup>th</sup> panel of Figure 4 shows a pronounced difference between the auroral power  
 389 estimates during the first and last periods of enhanced ionization. In the first time pe-  
 390 riod, between 19:45 and 19:48 UT, a difference of  $5 \text{ mWm}^{-2}$  is observed, whereas in the

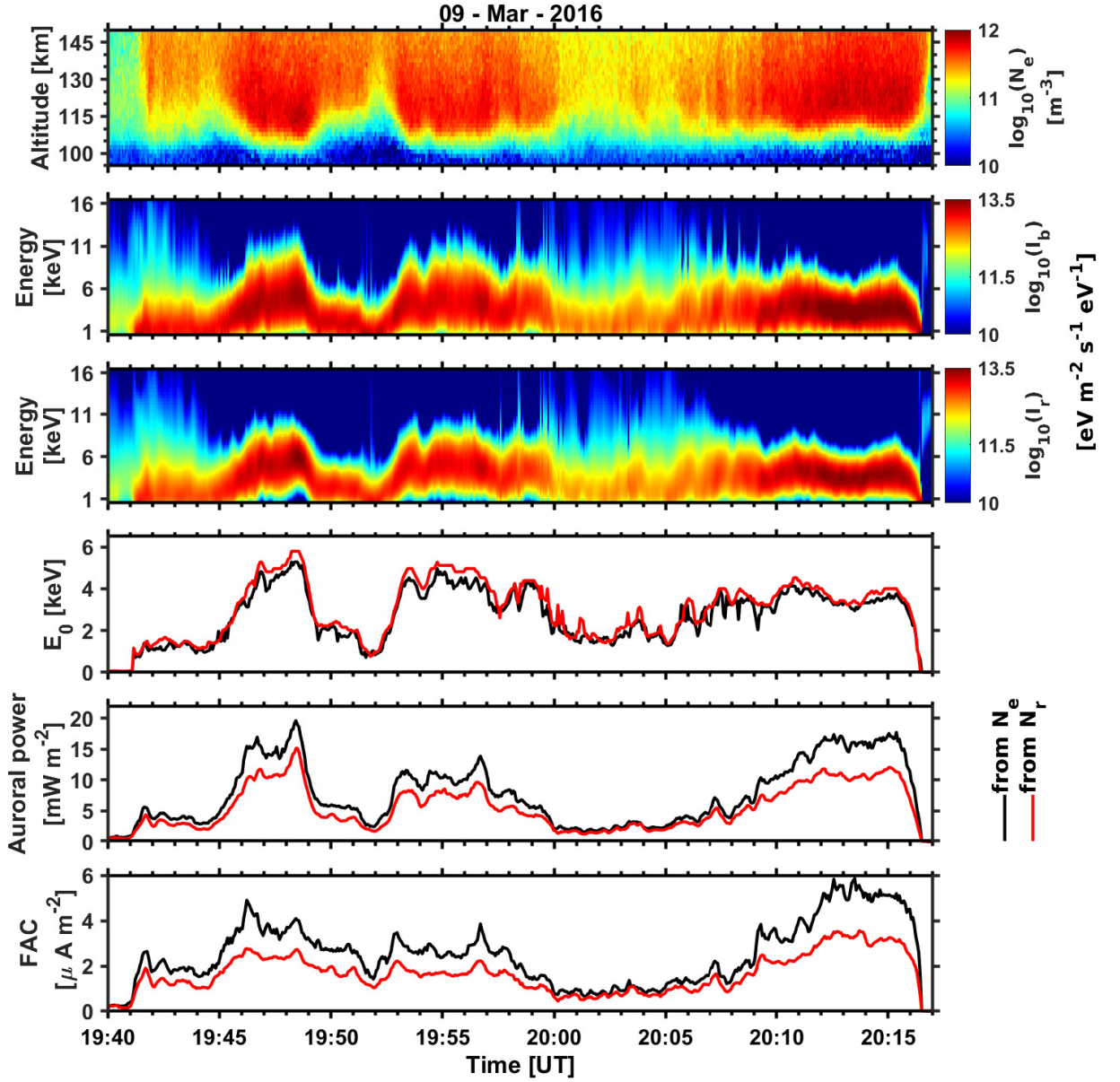


**Figure 4.** Comparison of ELSPEC fit results using raw density  $N_r$  and the BAFIM-fitted density  $N_e$  as inputs. Panels from top to bottom: The BAFIM-fitted  $N_e$ , the differential electron energy fluxes inverted from the BAFIM-fitted  $N_e$  ( $I_b$ ) and raw density ( $I_r$ ), peak energies ( $E_0$ ), auroral powers, and field-aligned currents (FAC). In panels 4-6, the black and red curves correspond to the BAFIM-fitted and raw electron density results, respectively.

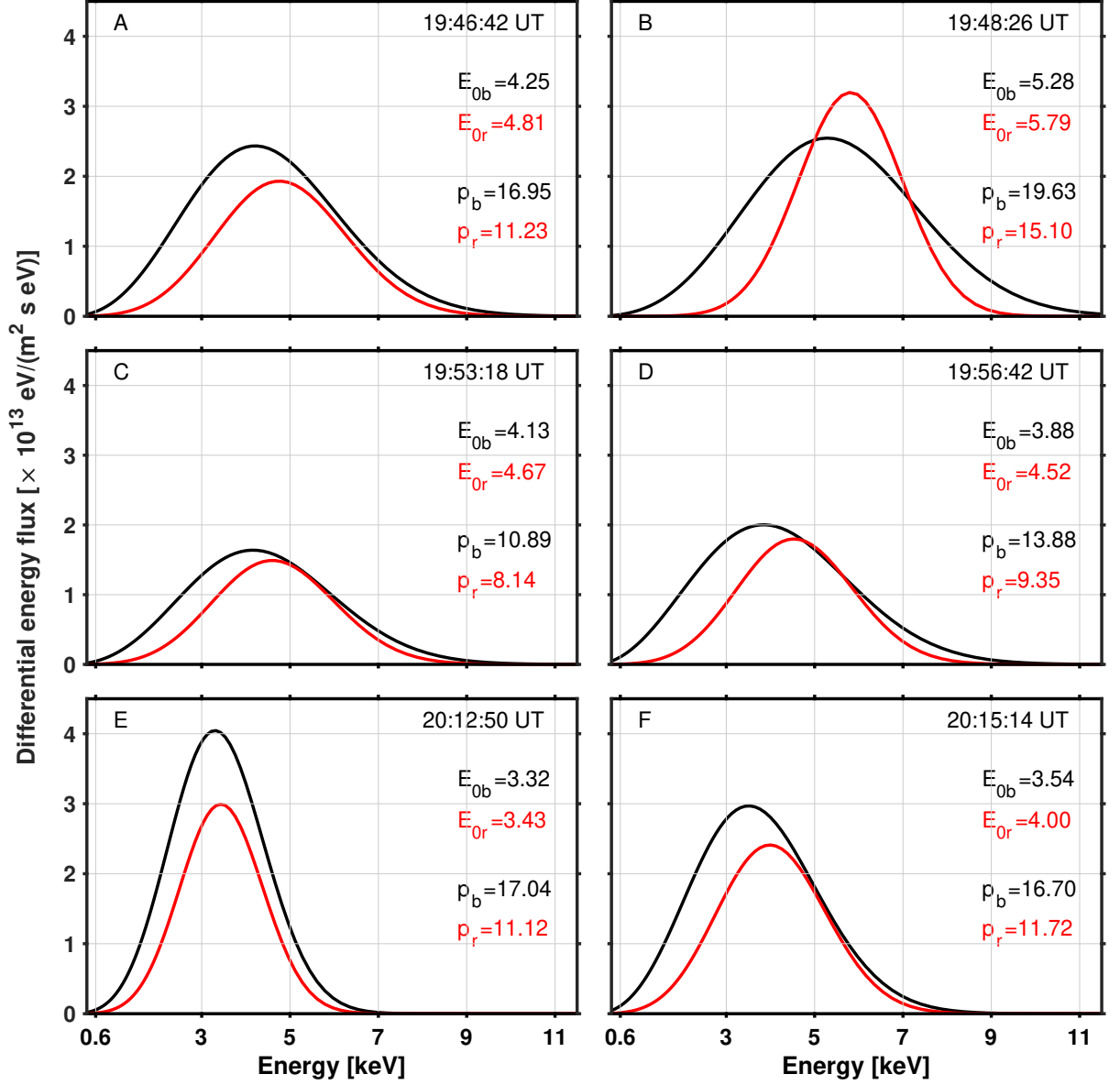


**Figure 5.** Comparison of selected differential energy flux estimates calculated from BAFIM-fitted electron density  $N_e$  (black) and raw electron density  $N_r$  (red).  $E_{ob}$  and  $P_b$  are the peak energies (in keV) and auroral power estimates (in mWm<sup>-2</sup>) calculated from the BAFIM-fitted  $N_e$ .  $E_{or}$  and  $P_r$  are the corresponding quantities calculated from the raw density  $N_r$ .

391 last time period, between 20:09 and 20:16 UT, the difference is about  $6 \text{ mWm}^{-2}$ . Dur-  
 392 ing both periods, the auroral power calculated from the BAFIM-fitted  $N_e$  exceeds its coun-  
 393 terpart calculated from raw density  $N_r$  by about 50%. The 6<sup>th</sup> panel of Figure 3 shows  
 394 a significant difference between the FAC estimates for a longer period of time, between  
 395 19:45 and 19:57 UT. Within the given time interval, the difference between the FAC es-  
 396 timates is about  $2 \mu\text{Am}^{-2}$  (70%). Between 20:09 and 20:15 a  $2.6 \mu\text{Am}^{-2}$  (65%) differ-  
 397 ence is observed. In general the total energy flux and number flux estimates obtained  
 398 from BAFIM  $N_e$  exceed those obtained from raw density  $N_r$  during each period of en-  
 399 hanced ionization. Detailed distribution of the differences in auroral power and FAC es-  
 400 timates across the entire data will be discussed in Section 4.5.

401 Figure 5 shows line plots of selected differential energy flux estimates derived from  
 402 the BAFIM-fitted  $N_e$  (black) and raw density  $N_r$  (red). The line plots in panels A - F  
 403 of the figure show energy spectra of the precipitating electrons that produce the corre-  
 404 sponding auroral arcs shown in panels A - F of Figure 2. The peak energies (in keV) and  
 405 auroral power estimates (in  $\text{mWm}^{-2}$ ) at the given time instants are also shown in the  
 406 figure. All the line plots distinctly demonstrate that the differential energy flux calcu-  
 407 lated from the BAFIM-fitted  $N_e$  contains larger energy flux below its peak energy than  
 408 its counterpart calculated from the raw electron density. In addition, the energy spec-  
 409 tra obtained from the raw electron density  $N_r$  shows narrower energy distribution as com-  
 410 pared to its counterpart calculated from the BAFIM-fitted  $N_e$ .

411 BAFIM-ELSPEC analysis results in Figure 5 (black curves) indicate that the bright  
 412 arcs inside the radar beam shown in Figure 2 are produced by precipitating electrons of  
 413 peak energies between 3 and 5 keV. In addition, the total energy flux of the electrons  
 414 that powers the arcs lies in the range between 10 and  $20 \text{ mWm}^{-2}$ . The  $20 \text{ mWm}^{-2}$  au-  
 415 roral power, the largest one here, corresponds to the bright auroral arc observed in the  
 416 early expansion phase of the first substorm, at about 19:48 UT, as shown in Figure 2.

#### 417 4.5 Electron energy spectra from the whole time interval

418 Figure 6 shows different parameters derived from the radar data of the entire event  
 419 that comprises the three substorm activities. In the first and second panels, we have the  
 420 BAFIM-fitted  $N_e$  and the corresponding differential energy flux results, respectively. The  
 421 peak energy, auroral power and FAC estimates are placed in the remaining panels from  
 422 top to bottom. In panels 3-5, the black and red curves represent parameters derived from  
 423 the BAFIM-fitted and raw electron density results, respectively.

424 Several ionization enhancements with different peak altitudes are shown in the elec-  
 425 tron density plot. Ionization enhancements shown before about 21:30 UT have peak alti-  
 426 tudes that lie between 110 and 120 km. Energy distributions of the precipitating elec-  
 427 trons that produce these enhancements were peaking between 3 and 5 keV, as shown in  
 428 the second and third panels. After 21:30 UT, mainly two enhanced ionization periods  
 429 are shown with lowered peak altitudes in the range between 100 and 106 km. The en-  
 430 hancements are produced by hardening of the precipitating electrons whose energies reach  
 431 as large as 21 keV, as shown in the second panel of the figure. The largest peak energy  
 432 and auroral power estimates of the entire event are about 18 keV and  $40 \text{ mWm}^{-2}$ , re-  
 433 spectively, corresponding to the bright and large auroral bulge observed in the post mid-  
 434 night sector during the recovery phase of the second substorm, as illustrated in panel I  
 435 and J of Figure 2. In general, the large ionization enhancements observed before and af-  
 436 ter 21:30 UT are produced by flux of electrons whose peak energy lies in the range 3 -  
 437 5 keV, and 5 - 18 keV, respectively. Moreover, several of the auroral structures observed  
 438 during each substorm event are characterized by inverted-V energy spectra structures.  
 439 The second panel of the figure shows these structures, for example, in the time intervals  
 440 19:45 - 19:50 UT, 22:01 - 22:10 UT and 22:45 - 23:00 UT, owing to rapid motion of au-  
 441 roral arcs across the radar beam as detailed in Section 3.

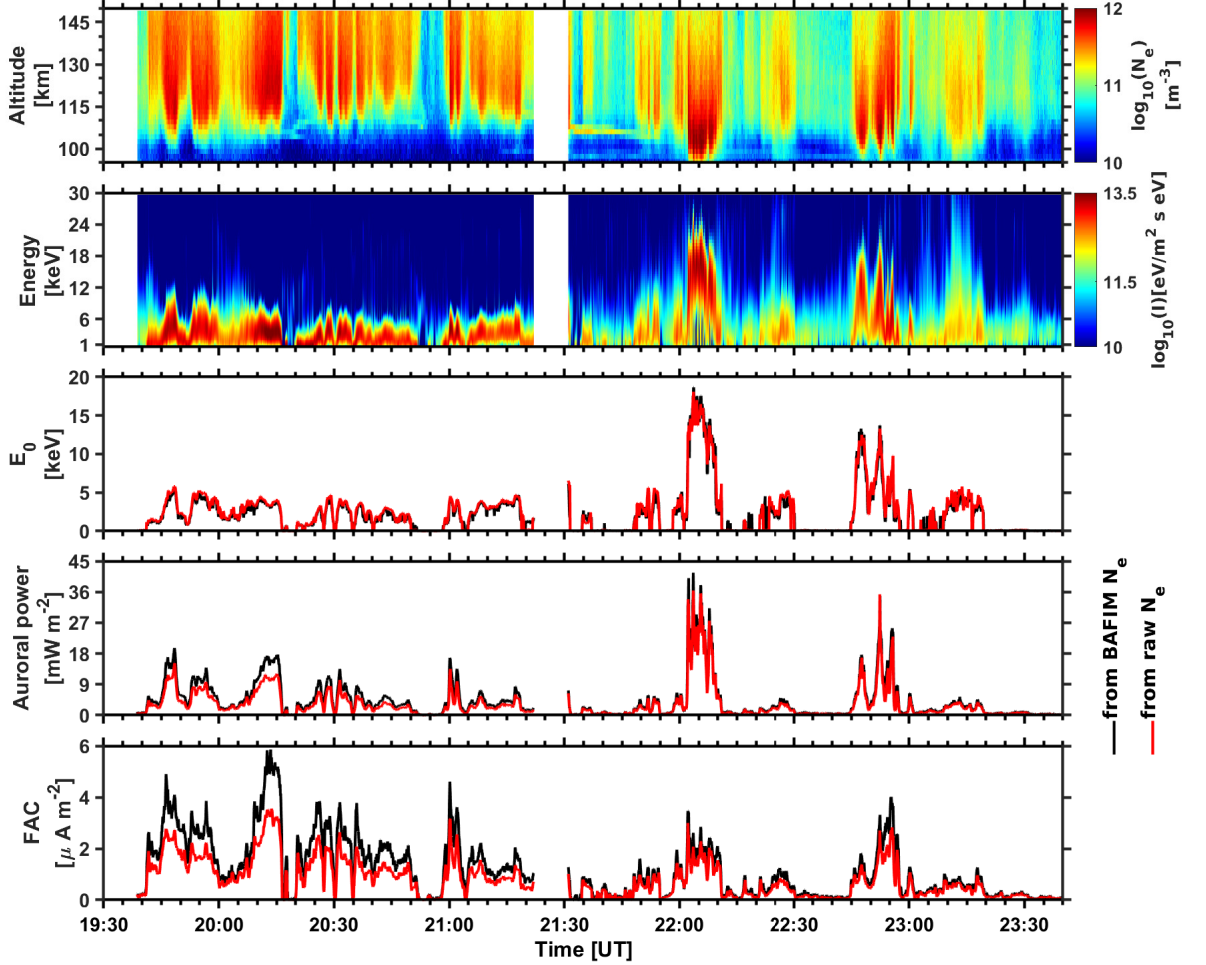


**Figure 6.** ELSPEC fit results during the whole event. Panels from top to bottom: BAFIM-fitted  $N_e$ , differential energy flux, peak energies, auroral powers, and FAC. In panels 3-5, the black and red curves correspond to ELSPEC analysis results using the BAFIM-fitted  $N_e$  and raw density  $N_r$ , respectively

442 The inference from the bottom two panels of Figure 6 is that the auroral power and  
 443 FAC estimates obtained from the BAFIM-fitted  $N_e$  significantly exceed their counter-  
 444 parts obtained from the raw density  $N_r$  during the first substorm before 21:30 UT. How-  
 445 ever, during the last two substorm periods after 21:30, the differences become smaller.  
 446 This is because, before 21:30 UT large flux of lower energy electrons deposit their en-  
 447 ergy at higher altitudes and heat the electron gas above the ion temperature. Whereas  
 448 for those periods after 21:30 UT, the electrons become sufficiently energetic and cause  
 449 enhanced ionization below 115 km altitude, where collisions balance the ion and elec-  
 450 tron temperatures. Electron temperature was sometimes higher than ion temperature  
 451 at high altitudes ( $> 120$  km) after 21:30 UT, but this has a relatively small effect on the  
 452 derivation of auroral power and FAC because peaks of the electron density altitude pro-  
 453 files were at lower altitudes.

454 Figure 7 presents distribution of the actual and percentage difference between the  
 455 auroral powers (left panel) and FAC (right panel) calculated from  $N_e$  and  $N_r$  data of the  
 456 whole time interval (4 hours). The differences are calculated only for time instances at

457 which the auroral power calculated from  $N_r$  is greater than  $3 \text{ mWm}^{-2}$ . The histograms  
 458 show that the differences between the auroral power estimates peak in the range  $0.5 -$   
 459  $2.5 \text{ mWm}^{-2}$  (30 - 45 %). For the FAC estimates, the peak difference is in the range  $0.25 -$   
 460  $0.5 \text{ } \mu\text{Am}^{-2}$  (45 - 55 %). The largest differences between the auroral power estimates  
 461 is about 75 %. In general, the histograms show that the auroral power and FAC esti-  
 462 mates calculated from  $N_e$  typically exceed those from  $N_r$ , but most of the times the dif-  
 463 ference is smaller than those extreme cases discussed in Section 4.4.

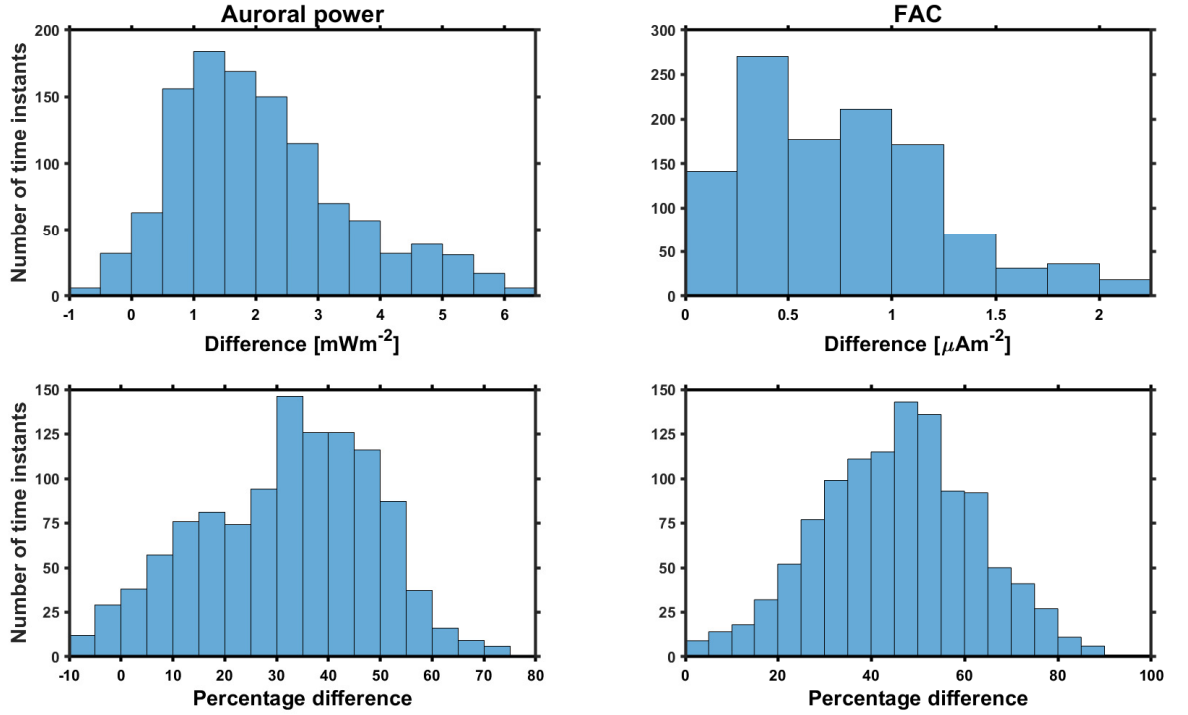


**Figure 7.** Distribution of the absolute and percentage differences in the auroral power (left panels) and FAC (right panels) estimates.

## 464 5 Comparison to optical observations

### 465 5.1 Auroral power from radar and blue molecular band emission intensity

466  
 467 We validate our radar analysis results by means of comparing radar observations  
 468 of auroral power with simultaneous, co-located observation of the blue 427.8 nm emis-  
 469 sion intensity, utilizing their proportionality relationship. The emission intensity data  
 470 used in this study is in arbitrary pixel count units without being corrected for dark cur-  
 471 rent leakage in the detectors (Nel, 2019), possible contributions from night time air-glow  
 472 emission, and atmospheric scattering of light from nearby sources. We subtract the back-  
 473 ground and scale the emission intensities to the same units with the radar data by means  
 474 of a linear least-square fit between the auroral power and the blue line emission inten-  
 475 sity. The emission intensity used in the linear fit is the median intensity of five pixels  
 476 found inside the radar beam. Equation 3 and Figure 8 show results of the linear fit be-  
 477 tween the blue line emission data and auroral power estimates calculated from BAFIM-

478 fitted  $N_e$ .

$$P = 0.0042I_{4278} - 3.8333, \quad (3)$$

479 where  $P$  is in  $\text{mWm}^{-2}$  and the constant term is attributed to the background data sources  
 480 in the optical data. Figure 8 demonstrates a very good linear relationship between the  
 481 427.8 nm emission intensity and the total energy flux of the precipitating electrons. For  
 482 this particular event, we calculated a cross-correlation coefficient value of 0.96 between  
 483 the auroral power and the 427.8 nm emission intensity.

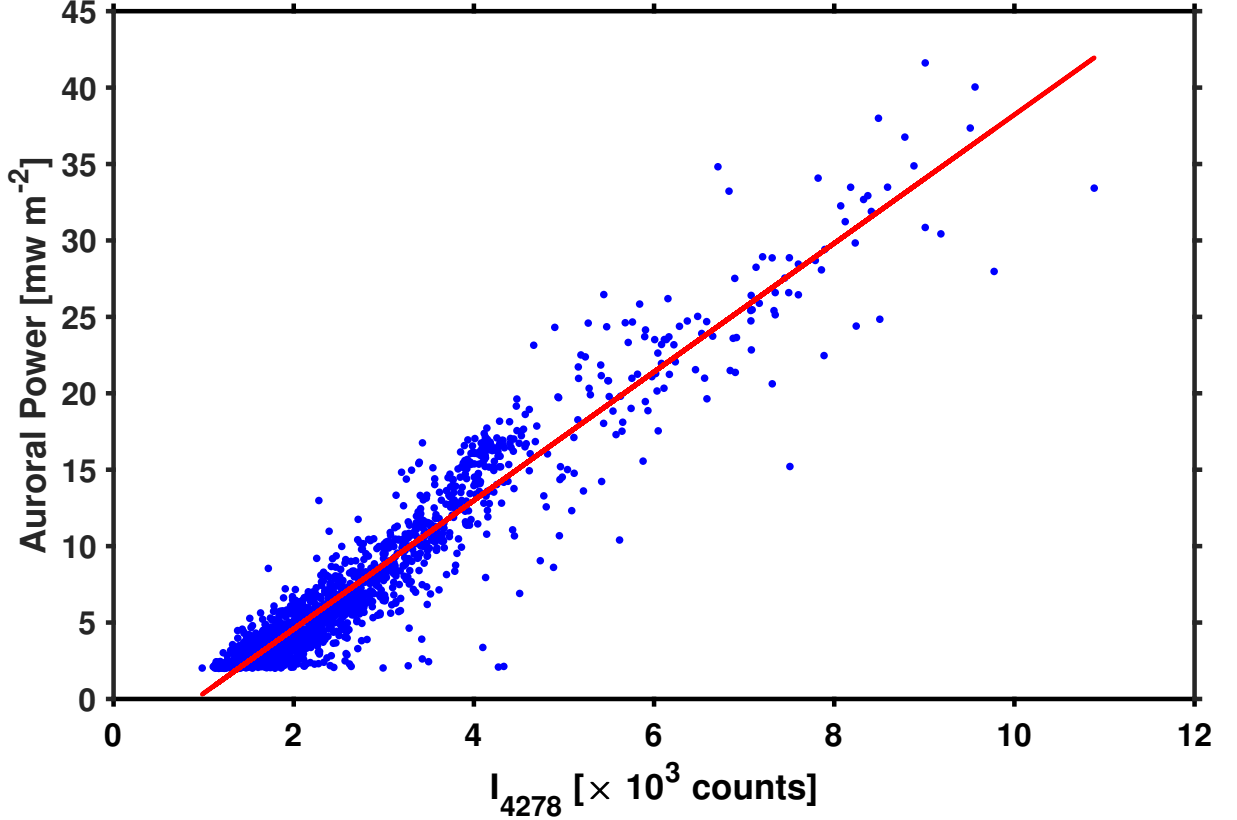


**Figure 8.** Fitting the blue line emission data to the auroral power calculated by ELSPEC using the BAFIM fitted electron density.

484 Comparison between the temporal variations of the scaled 427.8 nm emission in-  
 485 tensity and the auroral power is shown in the top panel of Figure 9. As shown in the fig-  
 486 ure, both large scale and small scale variations of the 427.8 nm emission intensity match  
 487 very well with variations in auroral power calculated from radar data. Furthermore, sharp  
 488 temporal gradients in the emission intensity are captured by the auroral power calcu-  
 489 lated from the radar data using the BAFIM-fitted electron density. By "sharp gradients"  
 490 we refer to variations in time-scales of the radar integration (4 s) in this context. Effects  
 491 of precipitation flux variations during a radar integration are discussed in Section 5.2.  
 492

493 There are some instances when the scaled emission intensity is smaller than the au-  
 494 roral power calculated from the radar data. This happens, for example, between 20:11  
 495 and 20:15 UT when the flux of about 1 keV electrons was large. Previous studies have  
 496 shown that the prompt emission rate of blue photons per unit deposited energy decreases

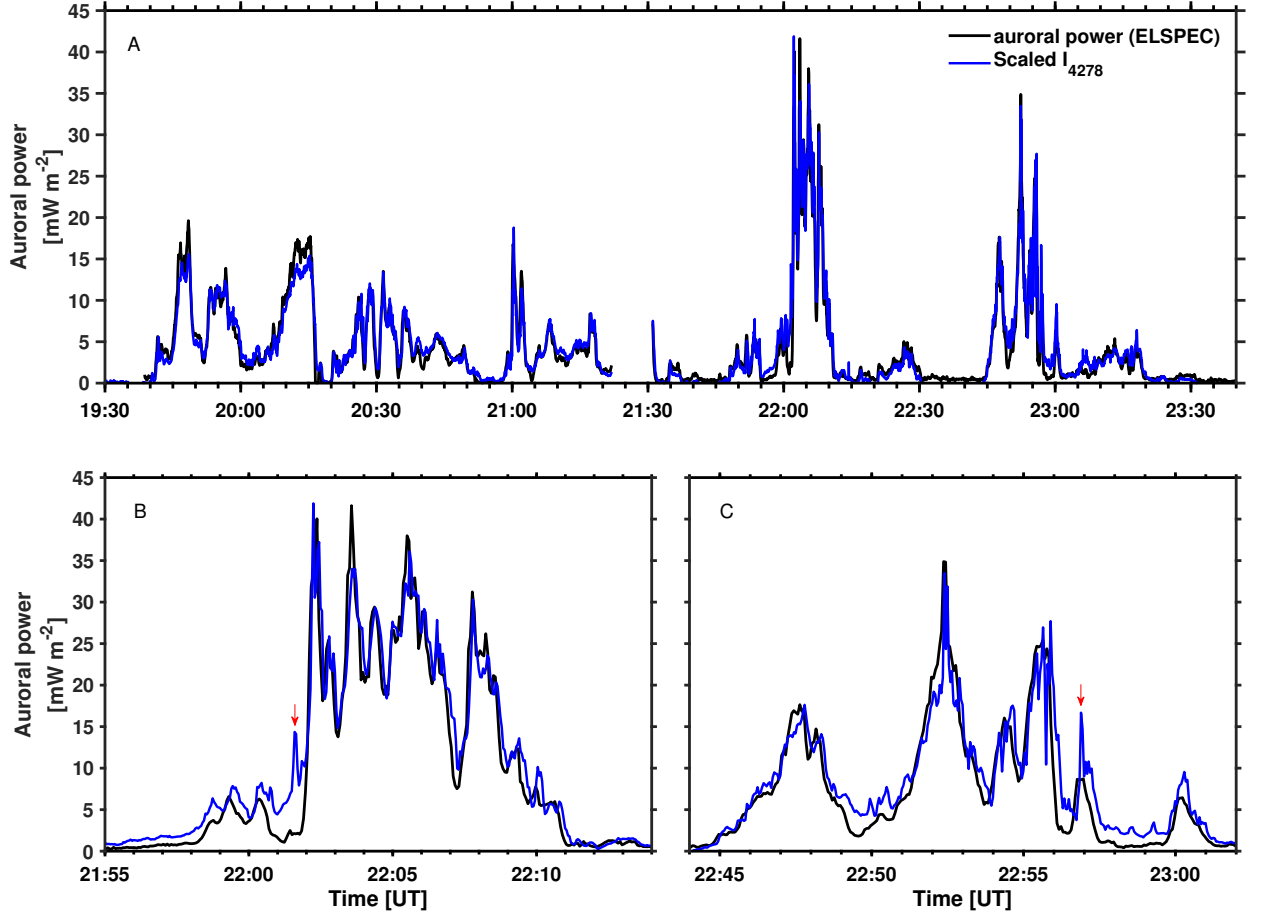


**Figure 9.** Panel A: Comparing the temporal variations of the auroral power (black) and the scaled emission intensity (blue). Panels B and C: selected periods from panel A.

497 with altitude and characteristic energy of the depositing electrons (Rees & Luckey, 1974;  
 498 Partamies et al., 2004). As a result, our scaled 427.8 nm emission intensities might be  
 499 underestimates of the auroral power during these time intervals. Another potential cause  
 500 of the discrepancy is overestimation of the auroral power by ELSPEC due to ion com-  
 501 position variations. The effect of ion composition variations was studied by Virtanen et  
 502 al. (2018), who found that the Sodankylä Ion and Neutral Chemistry (SIC) model (Tu-  
 503 runen et al., 2016) predicts enhanced and rapidly varying  $O_2^+$  to  $NO^+$  ion ratios dur-  
 504 ing electron precipitation, and ELSPEC analysis with  $O_2^+$  to  $NO^+$  ion ratio taken from  
 505 the International Reference Ionosphere (Bilitza et al., 2017) produced up to 20% larger  
 506 auroral powers than the corresponding analysis using SIC ion compositions in an event  
 507 study.

## 508 5.2 Effect of narrow auroral structures on ELSPEC analysis

509 Figure 9 also shows a few instances when the scaled emission intensity is clearly  
 510 larger than the auroral power calculated from radar data. For better visualization, se-  
 511 lected parts of the comparison graph which contain these time instants are shown sep-  
 512 arately in panels B and C of the Figure. Centered at each time instant, narrow FoV au-  
 513 roral images from three subsequent 3 s exposure times are shown in Figure 10. The first

514 one occurs between 22:01:35 UT and 22:01:41 UT (indicated by a red arrow in panel B  
 515 of Figure 9) when a thin auroral structure with rapidly varying intensity is within the  
 516 radar beam, as shown in the top panels of Figure 10. The images indicate that the radar  
 517 beam is not filled uniformly by the arc before and after 22:01:38 UT. In addition, a satel-  
 518 lite crossed the radar beam at 22:01:41, and light reflected from the satellite contributes  
 519 to the observed emission intensity. The satellite is marked with blue arrows in the Fig-  
 520 ure. Panel C of Figure 9 shows the next significant discrepancy at around 22:56:53 UT  
 521 (indicated by a red arrow), when the equatorward edge of an east west elongated arc en-  
 522 ters the radar beam and returns back within a time scale shorter than the radar inte-  
 gration time, as shown in the bottom panels of Figure 10.

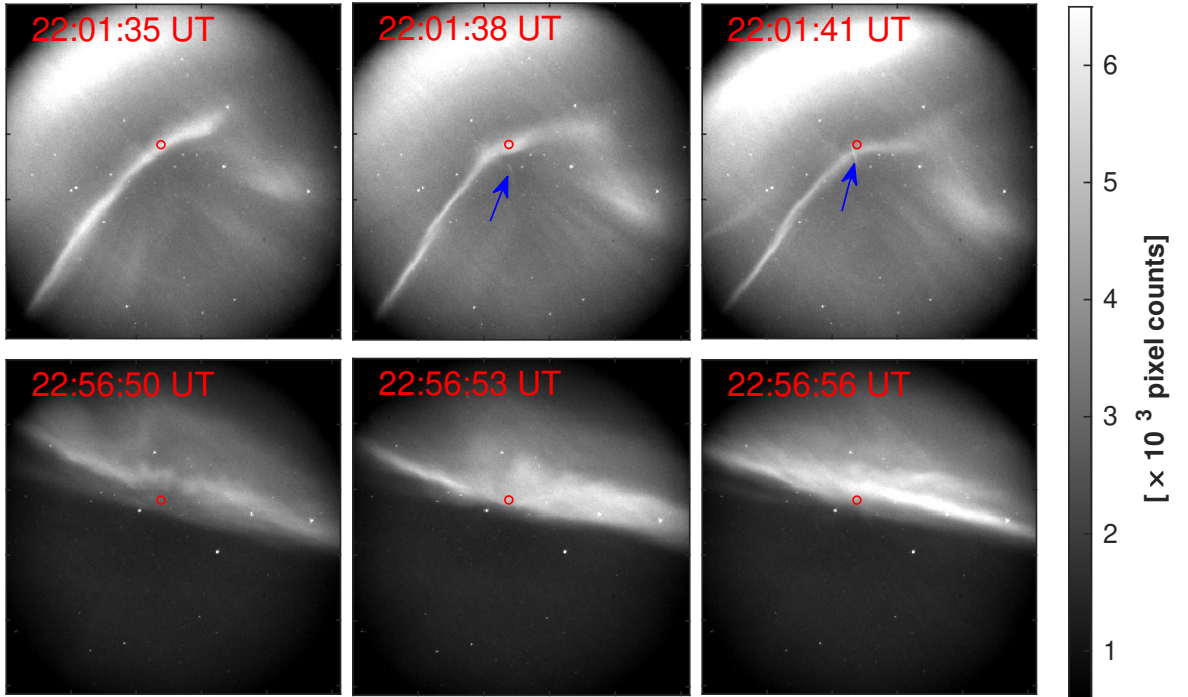


**Figure 10.** Narrow FoV auroral images at the given instants of time. The red circle represent the radar beam and the arrows indicate to a passing satellite.

523

524 The small scale structures and rapid variations are a probable reason for the dif-  
 525 ferences in these cases. The electron densities observed with the radar are averages of  
 526 electron density over the observation volume and integration time, while the optical ob-  
 527 servations are proportional to the ion production rate averaged over the radar beam and  
 528 exposure time. Our radar analysis then assumes that electron density is uniform within  
 529 the radar observing volume and finds a constant flux that leads to best fit between mod-  
 530 eled and observed electron density profiles. Violating the assumptions of uniform den-  
 531 sity within the observation volume and constant flux during the radar integration time  
 532 will readily lead to underestimation of the total flux. We thus have a reason to believe  
 533 that the optical observations are closer to the true mean auroral power within the radar  
 534 beam in these cases.

## 6 Discussion and Summary

This study demonstrates for the first time the applicability of a novel combination of two analysis methods (BAFIM and ELSPEC) for estimation of precipitating electron energy spectra, auroral power, and upward FAC from incoherent scatter radar measurements. The unique advantages of this combined analysis is utilization of the fitted electron density, instead of the raw electron density, with high time and range resolutions as input for the ELSPEC analysis. This removes a bias caused by electron heating that may have existed in previous high time resolution ISR observations which have relied on the raw electron density. Accurate electron energy spectra estimates are crucial for studies of small-scale, rapidly varying auroras, and incoherent scatter radars are currently the best available instruments for such observations.

The BAFIM-ELSPEC analysis method is applied to an auroral event containing three small substorms that occur in the pre-midnight and post-midnight sectors on 9 March 2016. The four-parameter fits of  $N_e$ ,  $T_e$ ,  $T_i$ , and  $V_i$  to the E region EISCAT UHF ISR data were performed with 4 s / 1.8 km resolutions by using the Bayesian Filtering Module (BAFIM) (Virtanen et al., 2021). We find that  $N_r$  is systematically smaller than  $N_e$  in the E region when electron precipitation heats the electron gas above the ion temperature. The effect is largest at the top of the E region, where  $N_e$  is up to 50 % larger than  $N_r$  above 130 km altitude, but significant differences are also observed down to 115 km.

When the fitted  $N_e$  is used in electron energy spectrum fits with ELSPEC (Virtanen et al., 2018), wider energy spectra and larger total fluxes are produced than in the corresponding analysis with  $N_r$  as input. Larger number fluxes are produced at the low energy end of the spectra in particular. Auroral power (total energy flux) integrated from the fitted energy spectra is up to 75 % larger than the estimates calculated with  $N_r$  as input. However, the distribution of the difference peaks at lower values between 30 - 45 %. Similarly, the upward FAC estimate is typically 45 - 55 % higher when the fitted  $N_e$  is used instead of the raw electron density. These results indicate that previous studies that have relied on the raw electron density may have significantly underestimated the auroral power and upward field-aligned current carried by the precipitating electrons.

Significant differences between the auroral power estimates are observed during the expansion phase of the first substorm which occurred in the pre-midnight sector in connection to flux of precipitating electrons with peak energies between 3 and 5 keV. The differences become insignificant when the precipitating electrons are sufficiently energetic to produce ionization at lower altitudes, in this study below 115 km. This happens, in this study, corresponding to the post-midnight auroral activities during the second and third substorm periods. The auroral power estimates corresponding to observed ionization enhancements during the night of 9 March 2016 were in the range of 3 - 40 mWm<sup>-2</sup>. These values are in accordance with several other previous studies (Stenbaek-Nielsen et al., 1998; Dahlgren et al., 2011; Kaeppler et al., 2015). The largest auroral power of the night, 40 mWm<sup>-2</sup>, was associated with a bright auroral bulge observed in the post-midnight sector as a result of precipitating electrons with peak energies as large as 18 keV.

The auroral powers calculated using the BAFIM-ELSPEC analysis combination were compared to column intensities of the optical 427.8 nm emission to validate the estimates. A linear correlation between the two were found, and the temporal evolution showed an excellent match. A few significant discrepancies during short time periods were found, but those were shown to correspond to situations when auroral structures narrower than the radar beam move across the beam, or when the electron energy spectrum changes considerably during a radar integration. In these cases, the observed discrepancies indicate that structures narrower than the radar beam and variations in time-scales shorter than the radar integration lead to underestimation of the total electron flux in ELSPEC.

586 Only electrons with energies larger than 1 keV are included in the estimates of au-  
 587 roral power and FAC in this study. ELSPEC cannot reliably estimate electron fluxes at  
 588 lower energies, because the low-energy electrons produce ionization above 150 km alti-  
 589 tude, where plasma convection and concentration of the long-lived  $O^+$  ions may be sig-  
 590 nificant. Ionization by the low-energy electrons can be seen in F region ISR measure-  
 591 ments, but it cannot be reliably used for the energy spectra inversion. As a consequence,  
 592 the FAC estimates of ELSPEC are merely lower limits, because contribution of low-energy  
 593 electrons to the total FAC could be significant. The auroral power estimates are expected  
 594 to be less affected, since the energy flux is typically dominated by auroral electrons with  
 595 energy greater than 1 keV.

596 Strong electric fields are sometimes known to exist adjacent to auroral arcs in the  
 597 ionosphere and they typically point toward the arc center (Lanchester et al., 1996; Aikio  
 598 et al., 2002). In the F region, the corresponding ion drifts take place along the auroral  
 599 arc, but with decreasing altitude the ion velocity turns more and more in the direction  
 600 of electric field due to Pedersen mobility in the E region, which means that the plasma  
 601 in the low density region outside of the arc may intrude to the more dense plasma in-  
 602 side the arc. This kind of behavior has been observed as an electron density depletion  
 603 around 125 km altitude by (Dahlgren et al., 2011) at the trailing edge of an arc. Such  
 604 density depletion would be incorrectly interpreted as very fast recombination by ELSPEC.  
 605 However, in the future, we will be able to measure the 2D horizontal plasma drift pat-  
 606 tern in the E and F regions by the EISCAT\_3D radar (McCrea et al., 2015) and take into  
 607 account the advection term in the continuity equation.

608 The present work uses 4 s time resolution due to limitations of the BAFIM-GUISDAP  
 609 software combination. Without this limitation we should be able to match the time res-  
 610 olution with duration of the alternating code cycle, which is 0.44 s in case of the arc1  
 611 experiment. It is also technically possible to run ELSPEC with sub-second resolution  
 612 data. As a matter of fact, the 0.44 s resolution energy spectra published by (Dahlgren  
 613 et al., 2011) were calculated by a software that was used as a starting point for ELSPEC  
 614 development.

## 615 Acknowledgments

616 We acknowledge the EISCAT Association for the incoherent scatter radar data used in  
 617 this study. EISCAT is an international association supported by research organizations  
 618 in China (CRIRP), Finland (SA), Japan (NIPR and STEL), Norway (NFR), Sweden (VR),  
 619 and the United Kingdom (NERC). EISCAT data are available for download from [https://  
 620 portal.eiscat.se/schedule/](https://portal.eiscat.se/schedule/). We thank T. Raita, Sodankylä Geophysical Observa-  
 621 tory, Finland, for the Kilpisjärvi Pulsation magnetometer data. We thank the institutes  
 622 who maintain the IMAGE Magnetometer Array: Tromsø Geophysical Observatory of  
 623 UiT the Arctic University of Norway (Norway), Finnish Meteorological Institute (Fin-  
 624 land), Institute of Geophysics Polish Academy of Sciences (Poland), GFZ German Re-  
 625 search Centre for Geosciences (Germany), Geological Survey of Sweden (Sweden), Swedish  
 626 Institute of Space Physics (Sweden), Sodankylä Geophysical Observatory of the Univer-  
 627 sity of Oulu (Finland), and Polar Geophysical Institute (Russia). This work is supported  
 628 by the Academy of Finland (301542) and the Kvantum institute of the University of Oulu.

## 629 References

- 630 Aikio, A. T., Lakkala, T., Kozlovsky, A., & Williams, P. J. S. (2002). Electric fields  
 631 and currents of stable drifting auroral arcs in the evening sector. *Journal of Geo-  
 632 physical Research: Space Physics*, 107(A12), SIA 3-1-SIA 3-14. doi: [https://doi  
 633 .org/10.1029/2001JA009172](https://doi.org/10.1029/2001JA009172)
- 634 Baron, M. J. (1977). The chatanika radar system. In A. Brekke (Ed.), *Radar probing  
 635 of the auroral plasma* (p. 103-141). Tromsø, Norway: Universitetsforlaget.

- 636 Bilitza, D., Altadill, D., Truhlik, V., Shubin, V., Galkin, I., Reinisch, B., & Huang,  
637 X. (2017). International Reference Ionosphere 2016: From ionospheric cli-  
638 mate to real-time weather predictions. *Space Weather*, *15*(2), 418-429. doi:  
639 10.1002/2016SW001593
- 640 Brekke, A., Hall, C., & Hansen, T. L. (1989, June). Auroral ionospheric conduc-  
641 tances during disturbed conditions. *Annales Geophysicae*, *7*, 269-280.
- 642 Burnham, K. P., & Anderson, D. R. (2002). *Model Selection and Multimodel Infer-*  
643 *ence* (2nd ed.). Springer.
- 644 Burns, C., Howarth, W., & Hargreaves, J. (1990). High-resolution incoherent  
645 scatter radar measurements during electron precipitation events. *Journal of At-*  
646 *mospheric and Terrestrial Physics*, *52*(3), 205 - 218. doi: [https://doi.org/10.1016/](https://doi.org/10.1016/0021-9169(90)90124-6)  
647 [0021-9169\(90\)90124-6](https://doi.org/10.1016/0021-9169(90)90124-6)
- 648 Carlson, C. W., Pfaff, R. F., & Watzin, J. G. (1998). The Fast auroral snapshot  
649 (FAST) mission. *Geophysical Research Letters*, *25*(12), 2013-2016. doi: [https://doi](https://doi.org/10.1029/98GL01592)  
650 [.org/10.1029/98GL01592](https://doi.org/10.1029/98GL01592)
- 651 Dahlgren, H., Gustavsson, B., Lanchester, B. S., Ivchenko, N., Brändström,  
652 U., Whiter, D. K., ... Marklund, G. (2011). Energy and flux variations  
653 across thin auroral arcs. *Annales Geophysicae*, *29*(10), 1699-1712. doi:  
654 <https://doi.org/10.5194/angeo-29-1699-2011>
- 655 Dombeck, J., Cattell, C., Prasad, N., Meeker, E., Hanson, E., & McFadden, J.  
656 (2018). Identification of auroral electron precipitation mechanism combina-  
657 tions and their relationships to net downgoing energy and number flux. *Jour-*  
658 *nal of Geophysical Research: Space Physics*, *123*(12), 10,064-10,089. doi:  
659 <https://doi.org/10.1029/2018JA025749>
- 660 Fang, X., Randall, C. E., Lummerzheim, D., Wang, W., Lu, G., Solomon, S. C., &  
661 Frahm, R. A. (2010). Parameterization of monoenergetic electron impact ion-  
662 ization. *Geophysical Research Letters*, *37*(22). doi: [https://doi.org/10.1029/](https://doi.org/10.1029/2010GL045406)  
663 [2010GL045406](https://doi.org/10.1029/2010GL045406)
- 664 Fujii, R., Nozawa, S., Sato, M., Matuura, N., Ono, T., Brekke, A., ... Hansen,  
665 T. L. (1995). Comparison between electron spectra calculated from EISCAT  
666 electron density profiles and those observed by the DMSP satellites. *Journal of*  
667 *geomagnetism and geoelectricity*, *47*(8), 771-782. doi: [https://doi.org/10.5636/](https://doi.org/10.5636/jgg.47.771)  
668 [jgg.47.771](https://doi.org/10.5636/jgg.47.771)
- 669 Hargreaves, J., & Devlin, T. (1990). Morning sector electron precipitation events  
670 observed by incoherent scatter radar. *Journal of Atmospheric and Terrestrial*  
671 *Physics*, *52*(3), 193 - 203. doi: [https://doi.org/10.1016/0021-9169\(90\)90123-5](https://doi.org/10.1016/0021-9169(90)90123-5)
- 672 Holt, J. M., Rhoda, D. A., Tetenbaum, D., & van Eyken, A. P. (1992, May-June).  
673 Optimal analysis of incoherent scatter radar data. *Radio Sci.*, *27*(3), 435-447. doi:  
674 <https://doi.org/10.1029/91RS02922>
- 675 Hsu, T.-S., & McPherron, R. L. (2012). A statistical analysis of substorm associated  
676 tail activity. *Advances in Space Research*, *50*(10), 1317-1343. doi: [https://doi.org/](https://doi.org/10.1016/j.asr.2012.06.034)  
677 [10.1016/j.asr.2012.06.034](https://doi.org/10.1016/j.asr.2012.06.034)
- 678 Hysell, D. L., Rodrigues, F. S., Chau, J. L., & Huba, J. D. (2008). Full profile in-  
679 coherent scatter analysis at Jicamarca. *Ann. Geophys.*, *26*, 59-75. doi: [10.5194/](https://doi.org/10.5194/angeo-26-59-2008)  
680 [angeo-26-59-2008](https://doi.org/10.5194/angeo-26-59-2008)
- 681 Kaeppler, S. R., Hampton, D. L., Nicolls, M. J., Strømme, A., Solomon, S. C.,  
682 Hecht, J. H., & Conde, M. G. (2015). An investigation comparing ground-based  
683 techniques that quantify auroral electron flux and conductance. *Journal of Geo-*  
684 *physical Research: Space Physics*, *120*(10), 9038-9056. doi: [https://doi.org/](https://doi.org/10.1002/2015JA021396)  
685 [10.1002/2015JA021396](https://doi.org/10.1002/2015JA021396)
- 686 Kallio, E. I., Pulkkinen, T. I., Koskinen, H. E. J., Viljanen, A., Slavin, J. A., &  
687 Ogilvie, K. (2000). Loading-unloading processes in the nightside ionosphere.  
688 *Geophysical Research Letters*, *27*(11), 1627-1630. doi: [https://doi.org/10.1029/](https://doi.org/10.1029/1999GL003694)  
689 [1999GL003694](https://doi.org/10.1029/1999GL003694)

- 690 Kirkwood, S. (1988). *SPECTRUM: A computer algorithm to derive the flux-energy*  
691 *spectrum of precipitating particles from EISCAT electron density profiles.*
- 692 Kirkwood, S., & Eliasson, L. (1990). Energetic particle precipitation in the sub-  
693 storm growth phase measured by EISCAT and Viking. *Journal of Geophysi-*  
694 *cal Research: Space Physics*, 95(A5), 6025-6037. doi: [https://doi.org/10.1029/](https://doi.org/10.1029/JA095iA05p06025)  
695 [JA095iA05p06025](https://doi.org/10.1029/JA095iA05p06025)
- 696 Kosch, M. J., Honary, F., del Pozo, C. F., Marple, S. R., & Hagfors, T. (2001).  
697 High-resolution maps of the characteristic energy of precipitating auroral particles.  
698 *Journal of Geophysical Research: Space Physics*, 106(A12), 28925-28937. doi:  
699 <https://doi.org/10.1029/2001JA900107>
- 700 Lanchester, B. S., Kaila, K., & McCrea, I. W. (1996). Relationship between  
701 large horizontal electric fields and auroral arc elements. *Journal of Geophysi-*  
702 *cal Research: Space Physics*, 101(A3), 5075-5084. doi: [https://doi.org/10.1029/](https://doi.org/10.1029/95JA02055)  
703 [95JA02055](https://doi.org/10.1029/95JA02055)
- 704 Lanchester, B. S., Palmer, J. R., Rees, M. H., Lummerzheim, D., Kaila, K., &  
705 Turunen, T. (1994). Energy flux and characteristic energy of an elemen-  
706 tal auroral structure. *Geophysical Research Letters*, 21(25), 2789-2792. doi:  
707 <https://doi.org/10.1029/94GL01764>
- 708 Lanchester, B. S., Rees, M. H., Lummerzheim, D., Otto, A., Frey, H. U., & Kaila,  
709 K. U. (1997). Large fluxes of auroral electrons in filaments of 100 m width.  
710 *Journal of Geophysical Research: Space Physics*, 102(A5), 9741-9748. doi:  
711 <https://doi.org/10.1029/97JA00231>
- 712 Lehtinen, M. S., & Häggström, I. (1987). A new modulation principle for incoher-  
713 ent scatter measurements. *Radio Sci.*, 22, 625-634. doi: [https://doi.org/10.1029/](https://doi.org/10.1029/RS022i004p00625)  
714 [RS022i004p00625](https://doi.org/10.1029/RS022i004p00625)
- 715 Lehtinen, M. S., & Huuskonen, A. (1996). General incoherent scatter analysis and  
716 GUIDAP. *Journal of Atmospheric and Terrestrial Physics*, 58(1), 435 - 452. doi:  
717 [https://doi.org/10.1016/0021-9169\(95\)00047-X](https://doi.org/10.1016/0021-9169(95)00047-X)
- 718 Lehtinen, M. S., Huuskonen, A., & Pirttilä, J. (1996, December). First experi-  
719 ences of full-profile analysis with GUIDAP. *Ann. Geophys.*, 14, 1487-1495. doi:  
720 <https://doi.org/10.1007/s00585-996-1487-3>
- 721 McCrea, I., Aikio, A., Alfonsi, L., Belova, E., Buchert, S., Clilverd, M., ... Vierinen,  
722 J. (2015). The science case for the EISCAT 3D radar. *Prog. Earth Planet. Sc.*,  
723 2(1). doi: 10.1186/s40645-015-0051-8
- 724 McPherron, R. L. (2005, Sep 01). Magnetic pulsations: Their sources and relation to  
725 solar wind and geomagnetic activity. *Surveys in Geophysics*, 26(5), 545-592. doi:  
726 [10.1007/s10712-005-1758-7](https://doi.org/10.1007/s10712-005-1758-7)
- 727 Mishin, V. V., Tsegmed, B., Klibanova, Y. Y., & Kurikalova, M. A. (2020). Burst  
728 geomagnetic pulsations as indicators of substorm expansion onsets during storms.  
729 *Journal of Geophysical Research: Space Physics*, 125(10), e2020JA028521. doi:  
730 <https://doi.org/10.1029/2020JA028521>
- 731 Nel, A. E. (2019). *Novel radar and optical observations of black auroras in the upper*  
732 *atmosphere* (Doctoral dissertation, North-West University). [https://repository](https://repository.nwu.ac.za/handle/10394/35266)  
733 [.nwu.ac.za/handle/10394/35266](https://repository.nwu.ac.za/handle/10394/35266).
- 734 Nel, A. E., Kosch, M. J., Whiter, D., Gustavsson, B., & Aslaksen, T. (2021, Jan 19).  
735 A new auroral phenomenon, the anti-black aurora. *Scientific Reports*, 11(1), 1829.  
736 doi: <https://doi.org/10.1038/s41598-021-81363-9>
- 737 Newell, T., Sotirelis, T., & Wing, S. (2009). Diffuse, monoenergetic, and broadband  
738 aurora: The global precipitation budget. *Journal of Geophysical Research: Space*  
739 *Physics*, 114(A9). doi: <https://doi.org/10.1029/2009JA014326>
- 740 Nose, M., Iyemori, T., Sugiura, M., & Kamei, T. (2015). *AE Index*. WDC for Geo-  
741 magnetism, Kyoto. doi: 10.17593/15031-54800
- 742 Ogawa, Y., Tanaka, Y., Kadokura, A., Hosokawa, K., Ebihara, Y., Motoba, T.,  
743 ... Fujii, R. (2020). Development of low-cost multi-wavelength imager

- 744 system for studies of aurora and airglow. *Polar Science*, *23*, 100501. doi:  
745 <https://doi.org/10.1016/j.polar.2019.100501>
- 746 Olson, J. V. (1999). Pi2 pulsations and substorm onsets: A review. *Journal of Geo-*  
747 *physical Research: Space Physics*, *104*(A8), 17499-17520. doi: <https://doi.org/10>  
748 [.1029/1999JA900086](https://doi.org/10.1029/1999JA900086)
- 749 Omholt, A. (1971). The electron aurora: Main characteristics and luminosity. In  
750 *Physics and chemistry in space* (p. 24-46). Springer Berlin Heidelberg. doi: 10  
751 [.1007/978-3-642-46269-6\\_2](https://doi.org/10.1007/978-3-642-46269-6_2)
- 752 Osepian, A., & Kirkwood, S. (1996). High-energy electron fluxes derived from EIS-  
753 CAT electron density profiles. *Journal of Atmospheric and Terrestrial Physics*,  
754 *58*(1), 479 - 487. doi: [https://doi.org/10.1016/0021-9169\(95\)00050-X](https://doi.org/10.1016/0021-9169(95)00050-X)
- 755 Partamies, N., Janhunen, P., Kauristie, K., Mäkinen, S., & Sergienko, T. (2004).  
756 Testing an inversion method for estimating electron energy fluxes from all-sky  
757 camera images. *Annales Geophysicae*, *22*(6), 1961-1971. doi: [https://doi.org/](https://doi.org/10.5194/angeo-22-1961-2004)  
758 [10.5194/angeo-22-1961-2004](https://doi.org/10.5194/angeo-22-1961-2004)
- 759 Rees, M. H. (1963). Auroral ionization and excitation by incident energetic elec-  
760 trons. *Planetary and Space Science*, *11*(10), 1209 - 1218. doi: <https://doi.org/10>  
761 [.1016/0032-0633\(63\)90252-6](https://doi.org/10.1016/0032-0633(63)90252-6)
- 762 Rees, M. H., & Luckey, D. (1974). Auroral electron energy derived from ratio of  
763 spectroscopic emissions 1. Model computations. *Journal of Geophysical Research*  
764 *(1896-1977)*, *79*(34), 5181-5186. doi: <https://doi.org/10.1029/JA079i034p05181>
- 765 Saito, T. (1969, December). Geomagnetic Pulsations. *Space Science Review*, *10*(3),  
766 319-412. doi: <https://doi.org/10.1007/BF00203620>
- 767 Sakurai, T., & Saito, T. (1976). Magnetic pulsation pi2 and substorm onset.  
768 *Planetary and Space Science*, *24*(6), 573 - 575. doi: [https://doi.org/10.1016/](https://doi.org/10.1016/0032-0633(76)90135-5)  
769 [0032-0633\(76\)90135-5](https://doi.org/10.1016/0032-0633(76)90135-5)
- 770 Semeter, J., & Kamalabadi, F. (2005). Determination of primary electron spectra  
771 from incoherent scatter radar measurements of the auroral E region. *Radio Sci-*  
772 *ence*, *40*(2). doi: <https://doi.org/10.1029/2004RS003042>
- 773 Sheehan, C. H., & St.-Maurice, J.-P. (2004). Dissociative recombination of  
774  $N_2^+$ ,  $O_2^+$ , and  $NO^+$ : Rate coefficients for ground state and vibrationally ex-  
775 cited ions. *Journal of Geophysical Research: Space Physics*, *109*(A3). doi:  
776 <https://doi.org/10.1029/2003JA010132>
- 777 Simon Wedlund, C., Lamy, H., Gustavsson, B., Sergienko, T., & Brändström, U.  
778 (2013). Estimating energy spectra of electron precipitation above auroral arcs  
779 from ground-based observations with radar and optics. *Journal of Geophysi-*  
780 *cal Research: Space Physics*, *118*(6), 3672-3691. doi: [https://doi.org/10.1002/](https://doi.org/10.1002/jgra.50347)  
781 [jgra.50347](https://doi.org/10.1002/jgra.50347)
- 782 Stenbaek-Nielsen, H. C., Hallinan, T. J., Osborne, D. L., Kimball, J., Chaston, C.,  
783 McFadden, J., ... Carlson, C. W. (1998). Aircraft observations conjugate to  
784 FAST: Auroral arc thicknesses. *Geophysical Research Letters*, *25*(12), 2073-2076.  
785 doi: <https://doi.org/10.1029/98GL01058>
- 786 Strickland, D. J., Hecht, J. H., Christensen, A. B., & Kelly, J. (1994). Relationship  
787 between energy flux Q and mean energy E of auroral electron spectra based on  
788 radar data from the 1987 CEDAR campaign at Sondre Stromfjord, Greenland.  
789 *Journal of Geophysical Research: Space Physics*, *99*(A10), 19467-19473. doi:  
790 <https://doi.org/10.1029/94JA01901>
- 791 Strickland, D. J., Meier, R. R., Hecht, J. H., & Christensen, A. B. (1989). Deducing  
792 composition and incident electron spectra from ground-based auroral optical mea-  
793 surements: Theory and model results. *Journal of Geophysical Research*, *94*(A10),  
794 13527. doi: <https://doi.org/10.1029/ja094ia10p13527>
- 795 Tanskanen, E. I. (2009). A comprehensive high-throughput analysis of substorms  
796 observed by IMAGE magnetometer network: Years 1993-2003 examined. *Journal*  
797 *of Geophysical Research: Space Physics*, *114*(A5). doi: <https://doi.org/10.1029/>

798 2008JA013682

799 Turunen, E., Kero, A., Verronen, P. T., Miyoshi, Y., Oyama, S.-I., & Saito, S.  
800 (2016). Mesospheric ozone destruction by high-energy electron precipitation  
801 associated with pulsating aurora. *J. Geophys. Res. Atmos.*, *121*, 11852-11861. doi:  
802 10.1002/2016JD025015

803 Virtanen, I. I., Gustavsson, B., Aikio, A., Kero, A., Asamura, K., & Ogawa, Y.  
804 (2018). Electron energy spectrum and auroral power estimation from incoherent  
805 scatter radar measurements. *Journal of Geophysical Research: Space Physics*,  
806 *123*(8), 6865-6887. doi: 10.1029/2018JA025636

807 Virtanen, I. I., Tesfaw, H. W., Roininen, L., Lasanen, S., & Aikio, A. (2021).  
808 Bayesian filtering in incoherent scatter plasma parameter fits. *Journal of Geo-*  
809 *physical Research: Space Physics*, *126*(3), e2020JA028700. doi: [https://doi.org/](https://doi.org/10.1029/2020JA028700)  
810 [10.1029/2020JA028700](https://doi.org/10.1029/2020JA028700)

811 Vondrak, R. R., & Baron, M. J. (1977). A method of obtaining the energy dis-  
812 tribution of auroral electrons from incoherent scatter radar measurements. In  
813 A. Brekke (Ed.), *Radar probing of the auroral plasma* (p. 315-330). Tromsø,  
814 Norway: Universitetsforlaget.

815 Wickwar, V. B., Lathuillere, C., Kofman, W., & Lejeune, G. (1981). Elevated elec-  
816 tron temperatures in the auroral E layer measured with the chatanika radar. *Jour-*  
817 *nal of Geophysical Research: Space Physics*, *86*(A6), 4721-4730. doi: [https://doi](https://doi.org/10.1029/JA086iA06p04721)  
818 [.org/10.1029/JA086iA06p04721](https://doi.org/10.1029/JA086iA06p04721)